

Preprint 02-2004

**Embedded crack vs. smeared crack  
models: A comparison of elementwise  
discontinuous crack path approaches with  
emphasis on mesh bias**

J. Mosler and G. Meschke

**Ruhr University Bochum**

This is a preprint of an article published in:  
*Computer Methods in Applied Mechanics and  
Engineering*, Vol. 193, Issues 30–32, 3351–3375 (2004)

# Embedded crack vs. smeared crack models: A comparison of elementwise discontinuous crack path approaches with emphasis on mesh bias

J. Mosler

G. Meschke

*Lehrstuhl für Technische Mechanik*

Ruhr University Bochum

*Universitätsstr. 150, D-44780 Bochum, Germany*

E-Mail: mosler@tm.bi.ruhr-uni-bochum.de

URL: [www.tm.bi.ruhr-uni-bochum.de/mosler](http://www.tm.bi.ruhr-uni-bochum.de/mosler)

*Institute for Structural Mechanics*

Ruhr University Bochum

*Universitätsstr. 150, D-44780 Bochum, Germany*

E-Mail: guenther.meschke@sd.ruhr-uni-bochum.de

URL: [www.sd.ruhr-uni-bochum.de](http://www.sd.ruhr-uni-bochum.de)

## SUMMARY

This paper is concerned with an analysis of the mesh dependence of results from numerical failure analyses using the Strong Discontinuity Approach (SDA) based on an analytical and numerical comparison with a standard plasticity model, pertaining to the classical fracture energy based smeared crack concept using a consistent characteristic length. The SDA is characterized by incorporating the kinematics of fractured solids locally within the finite element. The resulting jumps in the displacement field are captured by their corresponding singularly distributed strains. For the analytical and numerical study of the mesh dependence only mode I failure is considered. Analogies and differences of both finite element formulations are investigated and evaluated.

## 1 Introduction

Despite considerable progress made in the numerical analysis of strain softening materials, computational failure analysis of materials undergoing fracture processes such as cracking in cementitious and other quasi-brittle materials or shear failure zones occurring in metallic materials and in soils, still remains an issue of intensive and controversial discussion in the scientific community.

From the mathematical and numerical point of view, initiation of strain localization results in the loss of ellipticity of the governing (static) equations and a lack of invariance of the computational results with respect to the spatial discretization if softening continuum models are employed, see, e.g. [11] for a more detailed account. In the last decade, various enhanced constitutive models suitable for the regularization of ill-posed strain softening problems, such as nonlocal models [5, 31], gradient-enhanced models [12, 23] and COSSERAT continua [10, 38], have been proposed. These models eliminate the pathological influence of the discretization. Moreover, as was shown in [14], also the influence of the mesh orientation is reduced. Each of the enhanced models makes use of an internal length parameter related to the specific material. These approaches, however, require a sufficiently fine resolution of the localization zone to guarantee mesh objectivity. Consequently, the required computational costs may be prohibitive for large scale applications.

Alternative approaches, in which the multiscale character of the underlying problem is taken into account, have been proposed. One of the first publications on the incorporation of the final failure kinematics into standard finite elements goes back to JOHNSON & SCOTT [16]. In addition to continuous shape functions, they employed discontinuous shape functions in the respective finite element as well. A more detailed insight into the incorporation of strong displacement discontinuities within classical local elasto-plastic and elasto-damage continuum models was provided by SIMO, OLIVER & ARMERO [35]. This concept is based on a local decomposition of the displacement field into a continuous and a discontinuous part without enforcing  $C^0$  continuity of the field of the displacement discontinuities. In the Strong Discontinuity Approach (SDA), suggested by SIMO, OLIVER & ARMERO [35] and further elaborated by [2, 15, 22, 26, 32], among several others, the failure kinematics of solids, i.e. crack opening in brittle materials or sliding along shear failure zones in metallic materials, is approximated by means of discontinuous displacement fields locally embedded within the finite elements undergoing localization. Hence, no compatibility of the discontinuities across elements is required. Applying the Enhanced Assumed Strain (EAS) concept [36, 37], only the (enhanced) strains resulting from the discontinuous displacement field appear explicitly in the formulation (see [29, 34, 35]). Since the small scale (characterized by discontinuous displacement fields) is incorporated into the large scale (characterized by a smooth, compatible displacement field), this method is suitable for large scale structural applications. As far as the influence of the discretization on the computational results is concerned, numerical studies have been performed by [2, 26, 32].

More recently, the concept of discontinuous displacements has been incorporated within a finite element formulation based on the Partition of Unity concept [4]. In this approach, referred to as the Extended Finite Element Method (X-FEM), the displacement discontinuities are represented by means of additional degrees of freedom [18]. In case of crack analyses based on linear elastic fracture mechanics, the crack path is represented independently of the discretization. However, for cohesive crack models, a crucial issue relevant for the discretization influence remains the accurate determination of the crack direction at the crack tip.

In the present paper, the incompatible, local enhancement of the displacement field suggested by SIMO, OLIVER & ARMERO is analyzed with respect to mesh objectivity. More precisely, the influence of the mesh bias on numerical results from SDA based analyses is studied numerically as well as analytically. Only mode-I fracture is considered. Comparative evaluations are provided for rotating as well as for fixed discontinuities, using the specific formulation proposed in [20, 22], in which no crack path continuity is enforced, and considering constant strain elements. Since for constant strain elements, assuming fixed orientations of the cracks, this specific formulation and existing EAS formulations of the SDA [2, 7, 15, 28, 34, 40] are equivalent on the element level, the results obtained from the comparative evaluation at the element level also hold for other existing SDA-based models. A standard plasticity based smeared crack model without any nonlocal enhancements, using the consistent characteristic length according to OLIVER [25], is taken as a means of comparison.

The paper is organized as follows: In Section 2 the governing equations of single surface plasticity are summarized briefly. Section 3 is concerned with a fracture energy based regularization technique applying the consistent characteristic length according to OLIVER [25]. The strong discontinuity approach (SDA) is described in Section 4. Section 5 is concerned with an analytical comparison between the SDA and the smeared crack model. Analogies and differences of both finite element formulations are investigated and evaluated. Detailed numerical comparisons between both models are given in Section 6. The computations include the analysis of a notched concrete beam (Subsection 6.1) as well as the analysis of an L-shaped slab (Subsection 6.2).

## 2 Elasto-plastic modeling of mode-I failure

Rate-independent plasticity theory is used in this paper as a prototype model for mode-I failure in brittle materials for the comparative assessment. The respective set of governing equations of associative single surface plasticity for the geometrically linear theory is summarized in Fig. 1 (see e.g. [8, 17, 33]).

<p>1. Elastic constitutive equations:</p> $\boldsymbol{\sigma} = \mathbb{C} : (\boldsymbol{\varepsilon} - \boldsymbol{\varepsilon}^p) \quad \text{with:} \quad \begin{aligned} \mathbb{C} &:= \frac{\partial \boldsymbol{\sigma}}{\partial (\boldsymbol{\varepsilon} - \boldsymbol{\varepsilon}^p)} = \text{const.} \\ \boldsymbol{\varepsilon} &:= \nabla^s \mathbf{u} \end{aligned} \quad (1)$
<p>2. Space of admissible stress states (single surface plasticity):</p> $\mathbb{E}_{\boldsymbol{\sigma}} := \{(\boldsymbol{\sigma}, q) \in \mathbb{S} \times \mathbb{R} \mid \phi(\boldsymbol{\sigma}, q) \leq 0\} \quad (2)$
<p>3. associative flow rule:</p> $\dot{\boldsymbol{\varepsilon}}^p = \lambda \frac{\partial \phi}{\partial \boldsymbol{\sigma}} = \lambda \partial_{\boldsymbol{\sigma}} \phi \quad (3)$
<p>4. associative hardening law:</p> $\dot{q} = \partial_{\alpha} q \dot{\alpha} = -H \dot{\alpha} \quad \text{with:} \quad \dot{\alpha} = -\lambda \partial_q \phi \quad (4)$
<p>5. KUHN-TUCKER conditions</p> $\lambda \geq 0, \quad \phi(\boldsymbol{\sigma}, q) \leq 0, \quad \lambda \phi(\boldsymbol{\sigma}, q) = 0 \quad (5)$
<p>6. Consistency condition</p> $\lambda \dot{\phi} = 0 \quad (6)$

Figure 1: Classical rate-independent associative single surface plasticity with isotropic hardening/softening

For the modeling of cracks, the RANKINE criterion represents a suitable choice of the failure function  $\phi$ . From the definition of the maximum principle stress  $\sigma_A$

$$\sigma_A := \max_{1 \leq i \leq 3} \sigma_i, \quad \text{with} \quad \boldsymbol{\sigma} = \sum_{i=1}^3 \sigma_i \mathbf{n}_i \otimes \mathbf{n}_i, \quad (7)$$

together with the normalizing conditions  $\mathbf{n}_i \cdot \mathbf{n}_j = \delta_{ij}$ , the RANKINE failure surface can be recast in the form

$$\phi(\boldsymbol{\sigma}, \alpha) = (\mathbf{n}_A \otimes \mathbf{n}_A) : \boldsymbol{\sigma} - q(\alpha). \quad (8)$$

In Eq. (8)  $\mathbf{n}_A \otimes \mathbf{n}_A$  is the eigentensor corresponding to the eigenvalue  $\sigma_A$ .

## 3 Fracture energy concept

Without consideration of regularization techniques, results from finite element analyses based upon standard strain softening continuum models show a considerable mesh dependence, see

e.g. [11]. A simple, but nevertheless efficient concept to avoid the dependence of the results with respect to the resolution of the spatial discretization goes back to PIETRUSZCZAK & MROZ [30]. According to this model, the softening modulus  $H$  (see Eq. (4)) depends on the fracture energy per unit of crack surface  $\mathcal{G}_f$  and on the geometry of the respective finite element. From this assumption, the relationship

$$\mathcal{G}_f := \frac{E}{A_s} = \underbrace{\frac{E}{V}}_{g_f} l_c = \underbrace{\int_{\alpha=0}^{\alpha_u} q(\alpha) d\alpha}_{g_f} l_c \quad (9)$$

between the fracture energy  $\mathcal{G}_f$  and the fracture energy  $g_f$  per unit of volume can be derived. In Eq. (9)  $E$  represents the total dissipated energy in an element with the volume  $V$  required for the formation of a macro crack with the area  $A_s$ . According to Eq. (9), the relation between  $\mathcal{G}_f$  and  $g_f$  is provided by the characteristic length  $l_c$ .

Various definitions of this numerical length scale  $l_c$  have been proposed [9, 24, 25]. One formulation for  $l_c$  consistent with the chosen finite element discretization has been suggested by OLIVER [25]. In this model, the orientation of the crack within a finite element is taken into account. Considering two-dimensional finite elements, a crack corresponds to a jump in the displacement field, which is obtained as the limiting case of two singular lines converging to each other.

Introducing a singular line  $\partial_s\Omega$  within a domain  $\Omega$  implies the disjunct decomposition of the body

$$\partial_s\Omega \cup \Omega^+ \cup \Omega^- = \Omega \quad \text{and} \quad \partial_s\Omega \cap \Omega^+ \cap \Omega^- = \emptyset. \quad (10)$$

With the definition of the normal vector  $\mathbf{n}$  of the crack, which is assumed as a plane surface within the element, the set  $\Omega^+$  is specified as

$$\Omega^+ := \{\mathbf{X} \in \Omega \mid \mathbf{A} \in \partial_s\Omega, (\mathbf{X} - \mathbf{A}) \cdot \mathbf{n} > 0\}. \quad (11)$$

In what follows, all variables  $(\bullet)^+$  are associated with points in  $\Omega^+$ . With these definitions, the displacement field is assumed as

$$\mathbf{u} = \bar{\mathbf{u}} + [\![\mathbf{u}]\!] H_s. \quad (12)$$

In Eq. (12)  $\bar{\mathbf{u}}$  represents a smooth function ( $\bar{\mathbf{u}} \in \mathcal{C}^\infty(\mathbb{R}^3, \mathbb{R}^3)$ ),  $[\![\mathbf{u}]\!]$  denotes the displacement discontinuity in the point  $\mathbf{A}$  defined by

$$[\![\mathbf{u}]\!](\mathbf{A}) := \lim_{\mathbf{X}^+ \rightarrow \mathbf{A}} \mathbf{u}(\mathbf{X}^+) - \lim_{\mathbf{X}^- \rightarrow \mathbf{A}} \mathbf{u}(\mathbf{X}^-) \quad \forall \mathbf{A} \in \partial_s\Omega \quad (13)$$

and  $H_s$  is the HEAVISIDE function

$$H_s: \mathbb{R}^3 \rightarrow \mathbb{R} \\ \mathbf{X} \mapsto \begin{cases} 1 & \text{if } \mathbf{X} \in \Omega^+ \\ 0 & \text{if } \mathbf{X} \in \Omega^- \cup \partial_s\Omega. \end{cases} \quad (14)$$

Instead of the kinematic (12), OLIVER started with the approximation

$$[\![\mathbf{u}]\!] H_s \approx [\![\mathbf{u}]\!] \varphi, \quad \text{with} \quad \varphi \in \mathcal{C}^\infty(\mathbb{R}^3, \mathbb{R}). \quad (15)$$

The smooth ramp function  $\varphi$  was designed by means of the standard shape functions  $N_i(\boldsymbol{\xi})$  and specified as

$$\varphi = \sum_{i=1}^{n_{\Omega^+}} N_i(\boldsymbol{\xi}). \quad (16)$$

Consequently,  $\mathbf{u} \in C^0(\mathbb{R}^3, \mathbb{R}^3)$ . Since  $\text{supp}\varphi = \Omega$ , the displacement discontinuity  $[[\mathbf{u}]]$  is “smeared” over the domain  $\Omega$  (“smeared crack” model). From the definition of the fracture energy  $\mathcal{G}_f$ , together with the GAUSS theorem, the total dissipated energy  $E$  was computed in [25] for plane elements. The extension to the fully three-dimensional case yields [21], [19]

$$E = \int_{\Omega^e} \mathcal{G}_f \frac{\partial \varphi}{\partial \mathbf{X}} \cdot \mathbf{n} \, dV. \quad (17)$$

Combining Eq. (17) with Eq. (9), results in

$$l_c = (\overline{\nabla \varphi} \cdot \mathbf{n})^{-1}, \quad \text{with} \quad \overline{\nabla \varphi} := \frac{1}{V} \int_{\Omega} \nabla \varphi \, dV. \quad (18)$$

For constant strain finite elements the identity  $\overline{\nabla \varphi} = \nabla \varphi$  holds.

In Fig. 2b, the characteristic length  $l_c$  according to Eq. (18) obtained from the equilateral constant strain triangle (Fig. 2a) is plotted as a function of the crack orientation  $\theta$ . From Fig. 2b

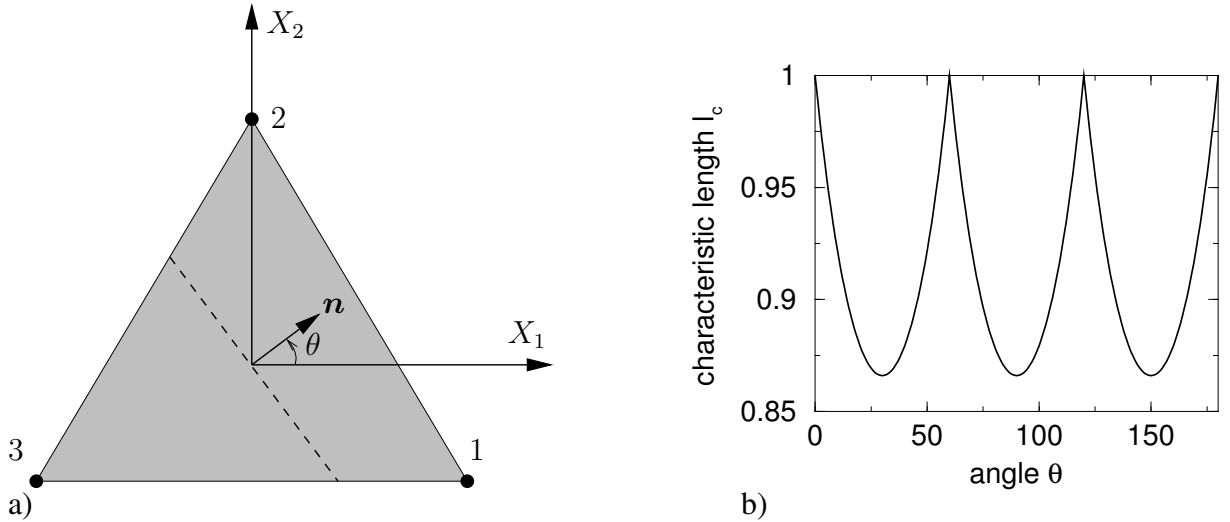


Figure 2: Equilateral triangle (edge length 1.0): a) Geometry, node numbering, crack orientation  $\mathbf{n}$  and global coordinate system, b) characteristic length  $l_c(\mathbf{n}(\theta))$  according to OLIVER [25]

follows, that  $l_c(\theta) \in C^0(2\pi, \mathbb{R}^+)$ . In more general cases, i.e. for quadrilateral and higher order elements,  $l_c(\theta) \notin C^0(2\pi, \mathbb{R}^+)$ .

**Remark 1:** For stress based crack formulations in the framework of plasticity and damage theory (see [22]), the topology of  $\partial_s \Omega$  is not fixed and depends on the stress tensor  $\boldsymbol{\sigma}$ . As a consequence,  $l_c = l_c(\boldsymbol{\sigma})$  has to be considered in the linearization in the context of the algorithmic formulation.

## 4 Elasto-plastic crack models considering embedded displacement discontinuities

In contrast to the formulation of  $l_c$  according to [25], based on the limiting case of two singular surfaces leading to jumps in the displacement field, the Strong Discontinuity Approach ([35],

[28]) is directly based upon the additive decomposition of the displacement field  $\mathbf{u}$  into a  $\mathcal{C}^0$  smooth function  $\bar{\mathbf{u}}$  and a discontinuous part  $\hat{\mathbf{u}}$

$$\mathbf{u}(\mathbf{X}) = \bar{\mathbf{u}}(\mathbf{X}) + \hat{\mathbf{u}}(\mathbf{X}), \quad (19)$$

with

$$\hat{\mathbf{u}}(\mathbf{X}) = \llbracket \mathbf{u} \rrbracket M_s(\mathbf{X}), \quad M_s(\mathbf{X}) = H_s(\mathbf{X}) - \varphi(\mathbf{X}). \quad (20)$$

The function  $M_s(\mathbf{X})$  is decomposed into a jump part, described by the Heaviside function  $H_s(\mathbf{X})$  and the smooth function  $\varphi(\mathbf{X})$  necessary to prescribe the DIRICHLET boundary conditions in terms of  $\bar{\mathbf{u}}$  (see [35] for further details). Fig. 3 shows two possible modes of the function  $M_s(\mathbf{X}) = H_s(\mathbf{X}) - \varphi(\mathbf{X})$  for a plane 4-node finite element [22]. Restricting the model to the

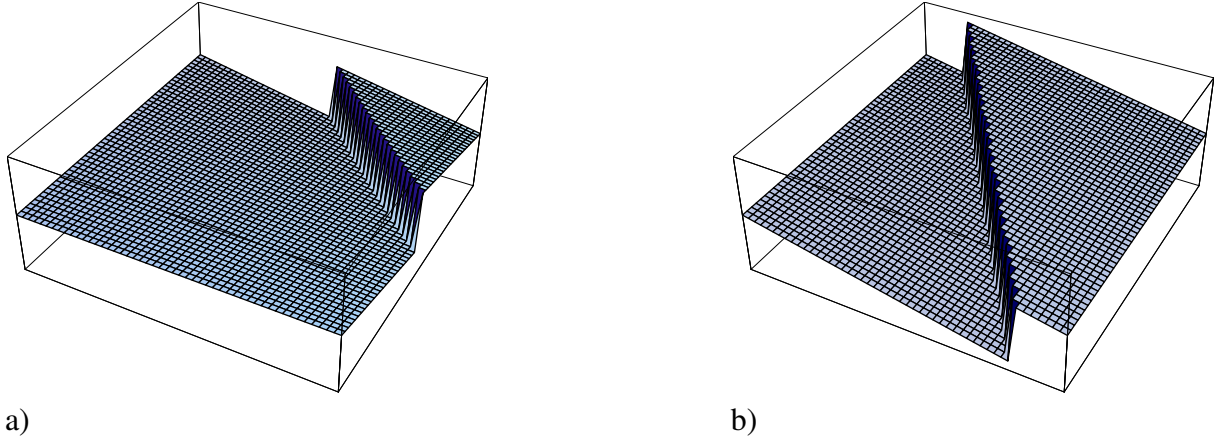


Figure 3: Two possible modes of discontinuous shape function  $M_s(\mathbf{X}) = H_s(\mathbf{X}) - \varphi(\mathbf{X})$  based on bi-linear functions for  $\varphi(\mathbf{X})$ : a) A crack cuts two adjacent sides of the finite element, b) a crack cuts two opposite sides of the finite element

geometrically linear theory, the strain tensor is obtained from Eq. (19) and (20) as

$$\varepsilon(\mathbf{u}) = \nabla^s \mathbf{u} = \nabla^s \bar{\mathbf{u}} - \underbrace{(\llbracket \mathbf{u} \rrbracket \otimes \nabla \varphi)^s}_{\tilde{\varepsilon}}, \quad \forall \mathbf{X} \in \Omega^\pm, \quad (21)$$

with

$$\llbracket \dot{\mathbf{u}} \rrbracket = \dot{\zeta} \mathbf{m}. \quad (22)$$

The assumption  $\nabla \llbracket \mathbf{u} \rrbracket = \mathbf{0}$  implicitly assumed in Eq. (21) can be motivated by the finite element implementation (see [3, 6, 22, 34]). Consequently, the amplitude of the displacement jump  $\zeta$  as well as its direction  $\mathbf{m}$  are taken as constant with respect to a local neighborhood. Since the RANKINE criterion is applied for the analysis of concrete cracking,  $\mathbf{m}$  coincides with  $\mathbf{n}_A$ .

**Remark 2:** The equivalence  $\mathbf{m} = \mathbf{n} = \mathbf{n}_A$  only holds for rotating crack approaches. For fixed crack models ( $\dot{\mathbf{n}} = \mathbf{0}$ ), this restriction would lead to an unrealistic increase of the shear component of the traction vector. Consequently, for fixed crack approaches an additional restriction for the shear component has to be applied. For mode I failure, a SDA-based fixed crack model is described in the Appendix.

Using the standard interpolation functions  $N_i$  for the design of the function  $\varphi(\mathbf{X})$ , the gradient  $\nabla \varphi$  is given as

$$\nabla \varphi = \sum_{i=1}^{n_{\Omega^+}} \frac{\partial N_i}{\partial \mathbf{X}}. \quad (23)$$

Since the additive decomposition (21) is formally identical to the standard Enhanced Assumed Strain concept (EAS), see e.g. [36, 37], the original implementation was based on this concept (see [29, 34, 35]). Hence, the stationarity condition of the respective two field functional reads

$$\begin{aligned} \int_{\Omega} \nabla \bar{\boldsymbol{\eta}} : \boldsymbol{\sigma}(\nabla^s \bar{\mathbf{u}}, \bar{\boldsymbol{\varepsilon}}) \, dV &= \int_{\Omega} \mathbf{f} \cdot \bar{\boldsymbol{\eta}} \, dV + \int_{\Gamma_{\sigma}} \mathbf{t}^* \cdot \bar{\boldsymbol{\eta}} \, d\Gamma \\ \int_{\Omega} \hat{\boldsymbol{\gamma}} : \boldsymbol{\sigma} \, d\Omega &= 0, \end{aligned} \quad (24)$$

with

$$\bar{\boldsymbol{\eta}} = \sum_{i=1}^{n_{\text{node}}} N_i \bar{\boldsymbol{\eta}}_i. \quad (25)$$

In Eq. (24)<sub>2</sub>  $\hat{\boldsymbol{\gamma}}$  represents the normalized variations of the enhanced strains,  $\mathbf{f}$  denotes prescribed body forces and  $\mathbf{t}^*$  the NEUMANN boundary conditions, respectively. Following a PETROV-GALERKIN discretization of the enhanced strains, SIMO & OLIVER specified  $\hat{\boldsymbol{\gamma}}$  as (see [34])

$$\hat{\boldsymbol{\gamma}} = -\frac{A_s}{V} (\mathbf{m} \otimes \mathbf{n})^{\text{sym}} + (\mathbf{m} \otimes \mathbf{n})^{\text{sym}} \delta_s, \quad \text{with} \quad \delta_s \mathbf{n} = \nabla H_s. \quad (26)$$

If constant strain elements are considered, Eq. (24)<sub>2</sub> yields

$$(\mathbf{m} \otimes \mathbf{n}) : \boldsymbol{\sigma} = (\mathbf{m} \otimes \mathbf{n}) : \boldsymbol{\sigma}|_{\partial_s \Omega}. \quad (27)$$

Hence, Eq. (24)<sub>2</sub> represents the weak form of traction continuity between  $\Omega^{\pm}$  and  $\partial_s \Omega$ . Introducing the definition  $q(\zeta) := (\mathbf{m} \otimes \mathbf{n}) : \boldsymbol{\sigma}|_{\partial_s \Omega}$ , the strong form of Eq. (24)<sub>2</sub> is formally identical to a failure condition

$$\phi(\boldsymbol{\sigma}, q) := (\mathbf{m} \otimes \mathbf{n}) : \boldsymbol{\sigma} - q(\zeta) = 0. \quad (28)$$

As a consequence, the algorithmic implementation can be restricted to the material point level (see [6, 20, 22]). In contrast to classical continuum models, Eq. (28) has the physical interpretation of a traction separation law connecting the component  $\mathbf{m} \cdot \mathbf{t}$  of the traction vector  $\mathbf{t}$  with the amplitude  $\zeta$  of the displacement discontinuity  $[[\mathbf{u}]]$ . For the case of the RANKINE criterion, Eq. (28) results in the traction separation law

$$\phi(\boldsymbol{\sigma}, \zeta) = (\mathbf{n}_A \otimes \mathbf{n}_A) : \boldsymbol{\sigma} - q(\zeta), \quad (29)$$

which relates the normal component of the stress vector  $\mathbf{t}$  to the normal component of the displacement jump  $[[\mathbf{u}]]$ . According to [35], the fracture energy can be computed as

$$\mathcal{G}_f = \int_{\zeta=0}^{\zeta_u} q(\zeta) \, d\zeta. \quad (30)$$

The amplitude of the displacement jump  $\zeta_u$  corresponds to an open macro-crack.

**Remark 3:** For constant strain elements Eq. (24)<sub>2</sub> is equivalent to Eq. (28). Consequently, no differences between the EAS formulation proposed in [2, 7, 15, 26–28, 34, 40] and the implementation suggested in [6, 20, 22] exist.

## 5 Comparative study of embedded discontinuity approaches and fracture energy based smeared crack models

This section contains a comparative study between the smeared crack and the embedded crack model as described in Sections 3 and 4. Since different implementations of embedded discontinuity approaches exist, the comparison is restricted to constant strain elements. Consequently, no differences between SDA-implementations formulated on the element level and implementations formulated on the material point level exist (see Remark 3). In contrast to [2, 7, 15, 26–28, 34, 40], a rotating crack approach ( $\dot{\mathbf{n}} \neq \mathbf{0}$ ) is followed [22]. Consequently, crack path continuity cannot be enforced. Since the discontinuous displacement field is approximated in an incompatible sense, the modeling of rotating discontinuities is admissible. As shown in [22], a rotating crack approach reduces locking effects observed in numerical analyses based on single fixed crack approaches.

The comparison is based on a single two-dimensional finite element as shown in Fig. 2 which is subjected to a state of plane stress characterized by

$$\boldsymbol{\sigma} := \sigma_A \mathbf{n}(\theta) \otimes \mathbf{n}(\theta) \quad \text{with} \quad \mathbf{n}^T(\theta) = [\cos \theta, \sin \theta]. \quad (31)$$

Hence, the vector  $\mathbf{n}_A$  corresponding to the maximum principle stress is given as

$$\mathbf{n}_A = \mathbf{n}(\theta). \quad (32)$$

The stress state assumed in Eq. (31) is sufficient for the present studies, since only the maximum principle stress enters the RANKINE failure criterion (29). For the elastic response of the material HOOKE's law, characterized by a constant tensor of elastic stiffness

$$\mathbb{C} = \frac{E}{1 + \nu} \mathbb{I}^{\text{sym}} + \frac{E \nu}{1 - \nu^2} \mathbf{1} \otimes \mathbf{1}, \quad (33)$$

is adopted. In Eq. (33)  $\mathbb{I}^{\text{sym}}$  denotes the symmetric fourth order identity tensor and  $\mathbf{1}$  represents the second order identity tensor, respectively. In what follows, for the sake of simplicity, it is assumed that the crack, characterized by the normal vector  $\mathbf{n}$ , is located in the centroid of the element. It should be noted, however, that the following study also holds for arbitrary locations of the crack within an element.

The gradient of  $\varphi$  according to Eq. (23) is computed as

$$\nabla \varphi = \begin{cases} \forall \theta \in (0^\circ, 60^\circ) & \nabla \varphi^T = [1.0, 0.57735] \\ \forall \theta \in (60^\circ, 120^\circ) & \nabla \varphi^T = [0, 1.1547] \\ \forall \theta \in (120^\circ, 180^\circ) & \nabla \varphi^T = [1.0, -0.57735]. \end{cases} \quad (34)$$

According to Eq. (18), the characteristic length  $l_c$  is obtained as

$$l_c = \begin{cases} \forall \theta \in (0^\circ, 60^\circ) & l_c = \frac{1}{\cos \theta + 0.57735 \sin \theta} \\ \forall \theta \in (60^\circ, 120^\circ) & l_c = \frac{1}{1.1547 \sin \theta} \\ \forall \theta \in (120^\circ, 180^\circ) & l_c = \frac{1}{\cos \theta - 0.57735 \sin \theta} \end{cases} \quad (35)$$

(see Fig. 2b).

For both models a linear softening law is used. Enforcing that the energy dissipated along the opening of a crack equals the fracture energy  $\mathcal{G}_f$ , yields the softening modulus of the SDA-model:

$$q(\zeta) = f_{\text{tu}} - H_\zeta \zeta \Rightarrow \mathcal{G}_f = \frac{1}{2} \frac{f_{\text{tu}}^2}{H_\zeta} \Rightarrow H_\zeta = \frac{1}{2} \frac{f_{\text{tu}}^2}{\mathcal{G}_f}, \quad (36)$$

with  $H_\zeta$  as the constant softening modulus governing the traction - crack opening relation. For the smeared crack concept, the softening modulus is obtained as

$$q(\alpha) = f_{tu} - H(\theta) \alpha \Rightarrow \mathcal{G}_f = \frac{1}{2} \frac{f_{tu}^2}{H(\theta)} l_c(\theta) \Rightarrow H = H_\zeta l_c(\theta). \quad (37)$$

Hence, the softening modulus  $H$  depends on the orientation of the normal vector of the crack surface via the characteristic length  $l_c$ .

Next, a discrete loading step leading to an increment of crack opening  $\Delta\zeta$  and  $\Delta\epsilon^{pl}(\theta)$  is considered. Introducing a trial state  $(\bullet)^{tr}$ , characterized by a purely elastic response within the considered increment  $\Delta t = t_{n+1} - t_n$  of the pseudo time  $t$ , together with an implicit backward EULER integration, the stress state at  $t_{n+1}$  is obtained from the fracture energy based smeared crack model (Eq. (1)) as

$$\boldsymbol{\sigma}_{n+1} = \boldsymbol{\sigma}_{n+1}^{tr} - \mathbb{C} : (\mathbf{n}(\theta) \otimes \mathbf{n}(\theta)) \Delta\lambda, \quad (38)$$

with the increment of the plastic multiplier  $\Delta\lambda := \lambda \Delta t$ . From the discrete yield condition  $\phi_{n+1} = 0$  the increment  $\Delta\lambda$  is obtained as

$$\Delta\lambda(\theta) = \frac{\phi^{tr}}{(\mathbf{n}(\theta) \otimes \mathbf{n}(\theta)) : \mathbb{C} : (\mathbf{n}(\theta) \otimes \mathbf{n}(\theta)) - H_\zeta l_c(\theta)}. \quad (39)$$

Analogously, the rate of the amplitude of the displacement jump  $\Delta\zeta$  resulting from the embedded crack model is obtained as

$$\Delta\zeta(\theta) = \frac{\phi^{tr}}{(\mathbf{n}(\theta) \otimes \mathbf{n}(\theta)) : \mathbb{C} : (\mathbf{n}(\theta) \otimes \nabla\varphi) - H_\zeta}. \quad (40)$$

From Eq. (39) the increment of the plastic strain tensor  $\Delta\epsilon^p$  and the corrector increment of the stress tensor  $\boldsymbol{\sigma}$  are computed for the smeared crack model as

$$\Delta\epsilon^{pl}(\theta) = (\mathbf{n}(\theta) \otimes \mathbf{n}(\theta)) \Delta\lambda(\theta) \quad \text{and} \quad \Delta\boldsymbol{\sigma}(\theta) = -\mathbb{C} : \Delta\epsilon^{pl}(\theta). \quad (41)$$

Analogously, the increments of the enhanced strains and the corrector increment of the stress tensor of the embedded crack model are given as

$$\Delta\tilde{\epsilon}(\theta) = (\mathbf{n}(\theta) \otimes \nabla\varphi)^{sym} \Delta\zeta(\theta) \quad \text{and} \quad \Delta\boldsymbol{\sigma}(\theta) = -\mathbb{C} : \Delta\tilde{\epsilon}(\theta). \quad (42)$$

For a graphical illustration of Eqs. (39) to (42), the material parameters contained in Tab. 1 are used. The trial stress is assumed as  $\sigma_A^{tr} = 1.5f_{tu}$ .

$E$	$\nu$	$G_f$	$f_{tu}$
1000 [kN/m <sup>2</sup> ]	0.3	0.01 [kNm/m <sup>2</sup> ]	1.0 [kN/m <sup>2</sup> ]

Table 1: Comparative study between smeared and embedded crack models: Material parameters

Fig. 4 illustrates the dependence of the components of  $\Delta\tilde{\epsilon}$  and  $\Delta\epsilon^p$  on the crack angle  $\theta$ . A comparison of  $\Delta\boldsymbol{\sigma}$  obtained from Eqs. (41) and (42), respectively, is illustrated in Fig. (5). Fig. 6 contains the rate of the amplitude of the displacement jump (40) vs. the plastic multiplier (39).

In contrast to the smeared crack model based on the characteristic length proposed in [25], the diagrams obtained from the embedded crack model in Fig. 4 are not continuous at  $\theta = 60^\circ$  and  $\theta = 120^\circ$ . The crack orientations  $\theta = 60^\circ$  and  $\theta = 120^\circ$  correspond to a crack

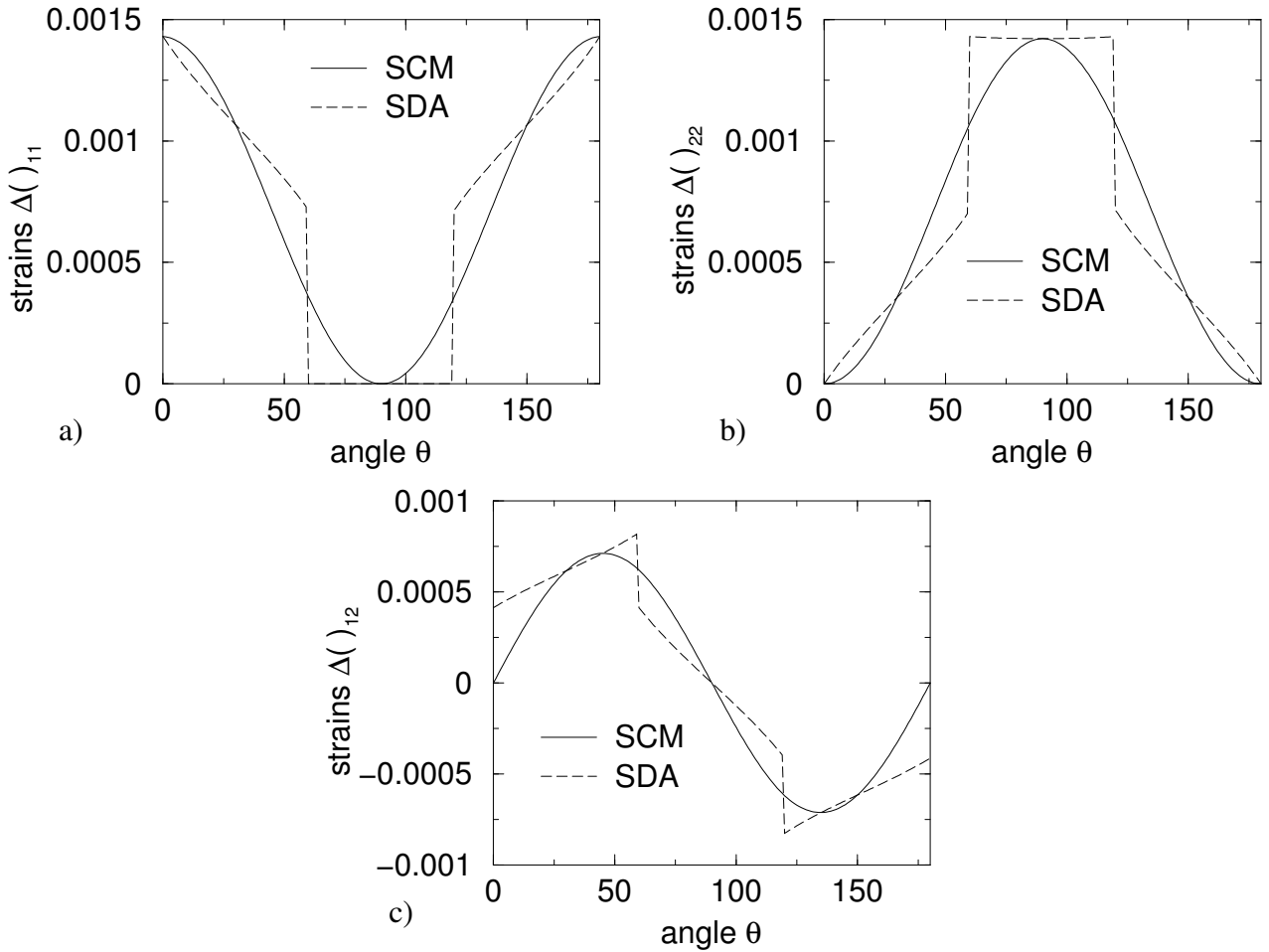


Figure 4: Comparative study between smeared crack models (SCM) and embedded crack models (SDA): Comparison of components of plastic strain increment  $\Delta\epsilon^P$  (fracture energy based smeared crack model) and increment of enhanced strain tensor  $\Delta\tilde{\epsilon}$  (embedded crack model) for a given loading step: a)  $\Delta\tilde{\epsilon}_{11}$  vs.  $\Delta\epsilon_{11}^P$ , b)  $\Delta\tilde{\epsilon}_{22}$  vs.  $\Delta\epsilon_{22}^P$ , c)  $\Delta\tilde{\epsilon}_{12}$  vs.  $\Delta\epsilon_{12}^P$

crossing element node 1 and 3, respectively (see Fig. 2a). For  $\theta = 60^\circ$  and  $\theta = 120^\circ$  the mapping  $\varphi$  has a discontinuity, which leads to non-smooth tensorial functions  $\Delta\tilde{\epsilon}(\theta)$ . For  $\theta = 30^\circ$ ,  $\theta = 90^\circ$  and  $\theta = 150^\circ$  the results of the SDA and the fracture energy based smeared crack model are equivalent. These orientations are characterized by cracks parallel to an edge of the finite element. As a consequence, the vectors  $\mathbf{n}$  and  $\nabla\varphi$  are linearly dependent and the PETROV-GALERKIN approximation of the enhanced strains degenerates to a GALERKIN type approximation. Since an isotropic elastic material is considered, the tensors  $\Delta\tilde{\epsilon}$  and  $\Delta\sigma$  are co-axial. Hence, the components of  $\Delta\sigma$  as shown in Fig. 5 correspond to the components of  $\Delta\tilde{\epsilon}$  (Fig. 4).

The dependence of the scalar variables  $\Delta\lambda$  and  $\Delta\zeta$  on the crack angle  $\theta$  is illustrated in Fig. 6. Both functions  $\Delta\lambda(\theta)$  and  $\Delta\zeta(\theta)$  agree qualitatively. However, since both variables  $\Delta\lambda$  and  $\Delta\zeta$  have a different physical relevance ( $\lambda =$  equivalent cracking strain,  $\zeta =$  crack width), the amplitudes are, except of the singular points  $\theta = 0^\circ$ ,  $60^\circ$  and  $120^\circ$ , different from each other.

Both stress-like softening variables  $q(\Delta\lambda)$  used in the smeared crack model and  $q(\Delta\zeta)$  used in the SDA based crack model represent the residual tensile strength. In Fig. 7, the increments of  $q(\Delta\lambda)$  and  $q(\Delta\zeta)$  are plotted as functions of the crack angle  $\theta$ . The distributions of  $q$  obtained from the two models are identical. Although the resulting stresses are not necessarily identical

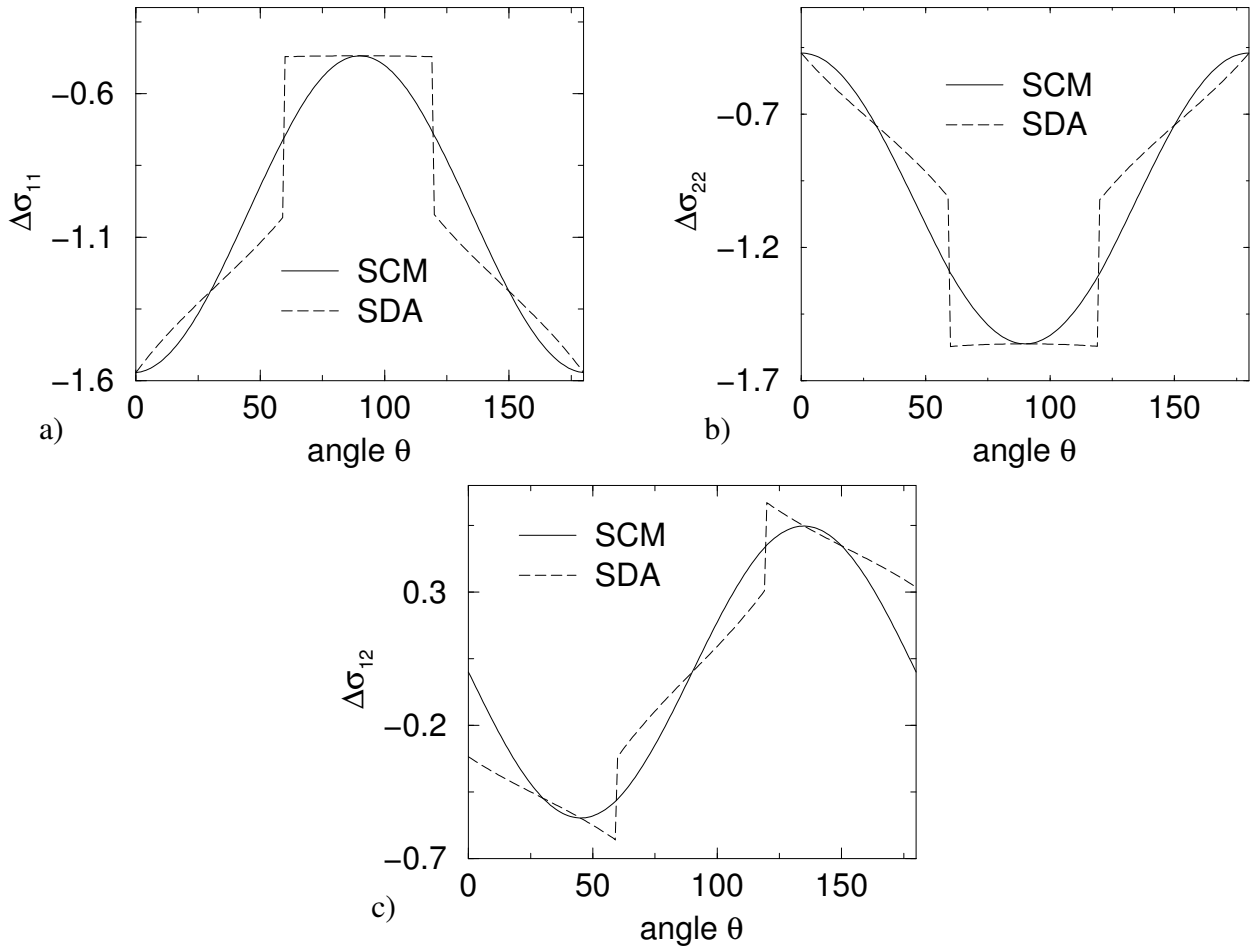


Figure 5: Comparative study between smeared crack models (SCM) and embedded crack models (SDA): Comparison of components of increment of stress tensor  $\Delta\sigma$  for a given loading step: a)  $\Delta\sigma_{11}$ , b)  $\Delta\sigma_{22}$ , c)  $\Delta\sigma_{12}$

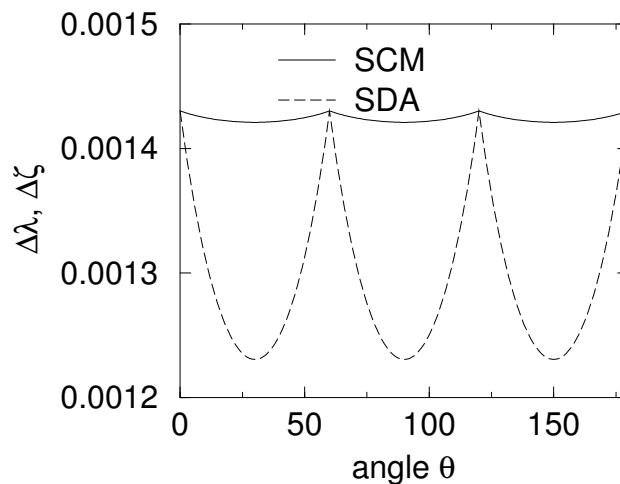


Figure 6: Comparative study between smeared crack models (SCM) and embedded crack models (SDA): Rate of the amplitude of the displacement jump  $\Delta\zeta$  vs. plastic multiplier  $\Delta\lambda$

(see Fig. 5), the equivalent softening response for both models at the onset of localization, as shown above, is an analytical indicator for a similar performance in structural failure analyses. In fact, as will be shown in Section 6 an almost identical dependence of the numerical results

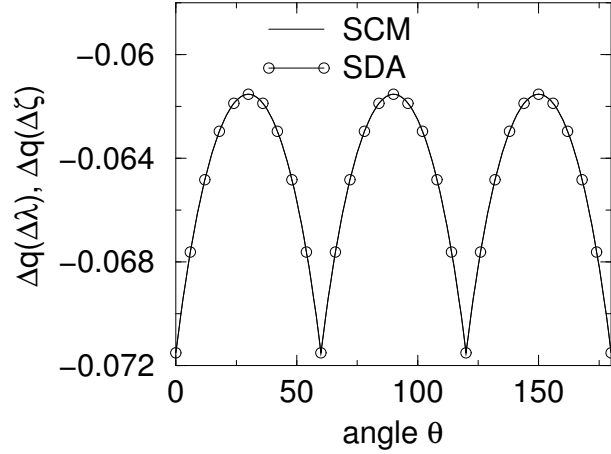


Figure 7: Comparative study between smeared crack models (SCM) and embedded crack models (SDA):  $\Delta q(\Delta\zeta)$  vs.  $\Delta q(\Delta\lambda)$

on the mesh bias is obtained from both models.

So far the comparative study was based on triangular finite elements as illustrated in Fig. 2a. In what follows, it will be shown that the results also hold for arbitrary positions of the crack as well as for general three-dimensional cases. For this purpose, the three-dimensional HOOKE's law, characterized by the free energy

$$\Psi(\varepsilon) = \frac{1}{2} \frac{E}{1+\nu} \varepsilon : \varepsilon + \frac{1}{2} \frac{E \nu}{(1+\nu)(1-2\nu)} \text{tr}^2 \varepsilon \quad (43)$$

is considered.

In what follows, it will be shown that  $\Delta q(\Delta\zeta) = \Delta q(\Delta\lambda)$ . Linearization of the internal stress-like variable  $q$  reads

$$-H_\zeta \Delta\zeta = \Delta q(\Delta\zeta) \quad \text{and} \quad \Delta q(\Delta\lambda) = -H(l_c) \Delta\lambda, \quad (44)$$

respectively. Eqs. (44), considering Eq. (39) and (40), yields

$$\begin{aligned} \Delta q(\Delta\zeta) &= -\phi^{\text{tr}} \left[ (\mathbf{n} \otimes \mathbf{n}) : \mathbb{C} : (\mathbf{n} \otimes \nabla\varphi) H_\zeta^{-1} - 1 \right]^{-1} \\ \Delta q(\Delta\lambda) &= -\phi^{\text{tr}} \left[ (\mathbf{n} \otimes \mathbf{n}) : \mathbb{C} : (\mathbf{n} \otimes \mathbf{n}) H_\zeta^{-1} l_c^{-1} - 1 \right]^{-1}. \end{aligned} \quad (45)$$

Consequently, for the identity  $\Delta q(\Delta\zeta) = \Delta q(\Delta\lambda)$ ,

$$(\mathbf{n} \otimes \mathbf{n}) : \mathbb{C} : (\mathbf{n} \otimes \nabla\varphi) \stackrel{!}{=} (\mathbf{n} \otimes \mathbf{n}) : \mathbb{C} : (\mathbf{n} \otimes \mathbf{n}) l_c^{-1}. \quad (46)$$

By inserting the linear elastic material law (43) into the left hand side of Eq. (46), the identity  $\Delta q(\Delta\zeta) = \Delta q(\Delta\lambda)$  is shown:

$$\begin{aligned} & (\mathbf{n} \otimes \mathbf{n}) : \mathbb{C} : (\mathbf{n} \otimes \nabla\varphi) \\ &= \left[ \frac{E}{1+\nu} (\mathbf{n} \otimes \mathbf{n}) + \frac{E \nu}{(1+\nu)(1-2\nu)} \mathbf{1} \right] : (\mathbf{n} \otimes \nabla\varphi) \\ &= \frac{E}{1+\nu} \mathbf{n} \cdot \nabla\varphi + \frac{E \nu}{(1+\nu)(1-2\nu)} \mathbf{n} \cdot \nabla\varphi \\ &= \frac{E(1-\nu)}{(1+\nu)(1-2\nu)} \mathbf{n} \cdot \nabla\varphi = \mathbb{C}_{1111} l_c^{-1} \\ &= (\mathbf{n} \otimes \mathbf{n}) : \mathbb{C} : (\mathbf{n} \otimes \mathbf{n}) l_c^{-1} \quad \square \end{aligned} \quad (47)$$

The last identity in Eq. (47) follows from the restriction to isotropy

$$(\mathbf{n} \otimes \mathbf{n}) : \mathbb{C} : (\mathbf{n} \otimes \mathbf{n}) = \text{const} \quad \forall \mathbf{n} \in \mathbb{R}^3 \text{ with } \|\mathbf{n}\|_2 = 1. \quad (48)$$

Note, that Eq. (47) does not imply

$$(\mathbf{n} \otimes \nabla \varphi)^{\text{sym}} = (\mathbf{n} \otimes \mathbf{n}) l_c^{-1}. \quad (49)$$

Since the left hand side of Eq. (49) defines the directions of the enhanced strains and the right hand side of Eq. (49) defines the directions of the plastic strains, respectively,  $\tilde{\varepsilon} \neq \varepsilon^p$ . From Eq. (44) and (47) follows the equivalence

$$\Delta \zeta = l_c \Delta \lambda. \quad (50)$$

Eq. (50) relates the plastic multiplier according to the smeared crack concept with the amplitude of the displacement jump. Hence,  $\Delta \lambda$  represents an equivalent crack strain obtained from homogenization of the increment of the displacement jump amplitude  $\zeta$ .

It should be noted, that the characteristic length concept according to OLIVER is based on a modification of the softening modulus via the scalar valued variable  $l_c$  and consequently, this approach is restricted to isotropy. In contrast, the embedded displacement discontinuity approach is based on the tensor of enhanced strains  $\tilde{\varepsilon}$  which, which allows its application also for the analyses of anisotropic materials. Hence, the identical evolution of softening is restricted to isotropic materials.

**Remark 4:** In most of the existing SDA formulations a crack path continuity is enforced [3, 13, 15, 28]. However, 3D formulations of the SDA without enforcing crack path continuity also have been proposed [22, 39, 40]. A comparison between finite element formulations with crack path continuity and without crack path continuity can be found in [1, 15]. In these references the influence of the crack path continuity on the computations is demonstrated. However, for CST-elements, crack path continuity can also be enforced for the fracture energy model based on the characteristic length according to OLIVER [25].

**Remark 5:** In this section, the equivalence of the softening evolution has been shown for rotating crack approaches. The Appendix of this paper contains an analytical comparison between the smeared crack model and the embedded displacement discontinuity approach for a fixed crack concept ( $\dot{\mathbf{n}} = \mathbf{0}$ ).

## 6 Numerical assessment of mesh dependence

In this section the mesh dependence of the SDA is analyzed numerically. For this purpose, two different examples are computed by means of the embedded crack model. The results are compared with the classical fracture energy based smeared crack model using the consistent characteristic length according to OLIVER. For a detailed description of the specific implementation of the rotating embedded crack model, we refer to [22].

In Subsection 6.1 a notched concrete beam is analyzed numerically. According to Remark 3, the applied implementation of the SDA model proposed in [22] is equivalent to the originally suggested algorithmic formulation in [2, 7, 15, 26–28, 34, 40] for triangular or tetrahedral elements using static condensation. Consequently, 3 node CST elements are used in this numerical study. For the purpose of comparison, a re-analysis is performed using 4 node quadrilateral elements. Subsection 6.2 contains a numerical analysis of an L-shaped slab.

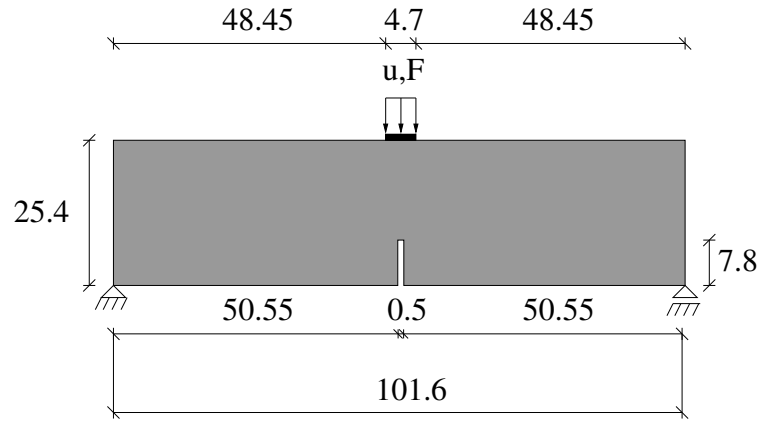


Figure 8: Finite element analysis of a notched concrete beam: Dimensions (in [cm]); thickness of the beam 0.127 m

Table 2: Finite element analysis of a notched concrete beam: Material parameters

Young modulus	$E$	$4.36 \cdot 10^3$	$\text{kN/cm}^2$
Poisson ratio	$\nu$	0.2	-
tensile strength	$f_{\text{tu}}$	0.4	$\text{kN/cm}^2$
Fracture energy	$\mathcal{G}_f$	$1.195 \cdot 10^{-3}$	$\text{kN cm/cm}^2$

## 6.1 Notched concrete beam

The geometry together with the loading and the DIRICHLET boundary conditions of the notched concrete beam are contained in Figure 8. The material parameters are contained in Table 2. Loading on top of the beam was applied by incrementally increasing nodal displacements along the width of the loading platen. The softening behavior of the RANKINE-type failure surface after onset of cracking is assumed to follow the exponential law

$$q(\alpha) = f_{\text{tu}} \exp \left[ -\alpha \frac{f_{\text{tu}}}{\mathcal{G}_f} \right], \quad (51)$$

where  $\mathcal{G}_f$  denotes the specific fracture energy of concrete in tension and  $f_{\text{tu}}$  is the uniaxial tensile strength of concrete. Convergence is checked according to the criterion

$$\frac{\|\mathbf{r}_i - \mathbf{r}_e\|_\infty}{\|\mathbf{r}_e\|_\infty} < 10^{-6}, \quad (52)$$

where  $\mathbf{r}_i$  ( $\mathbf{r}_e$ ) is the vector of internal (external) forces. For the analysis of the mesh dependence, 6 different discretizations are considered (see Fig. 9). Starting with the finite element mesh  $0^\circ$ , whose element edges are aligned with the analytical solution of the crack topology, the mesh bias is changed up to  $10^\circ$  in steps of  $2^\circ$ . The finite element discretizations used for the triangular elements were generated by subdividing each quadrilateral element into two triangles.

**Remark 6:** As shown in [22], a numerical analysis of the notched concrete beam by means of a fixed crack SDA-based finite element formulation (single crack) leads to a misprediction of the crack orientation resulting in locking effects. These drawbacks are eliminated using a rotating crack approach.

Figure 10 contains the distribution of the internal variable  $|\zeta|$ , which reflects the crack width, obtained from the embedded displacement discontinuity model using 3 node CST elements.

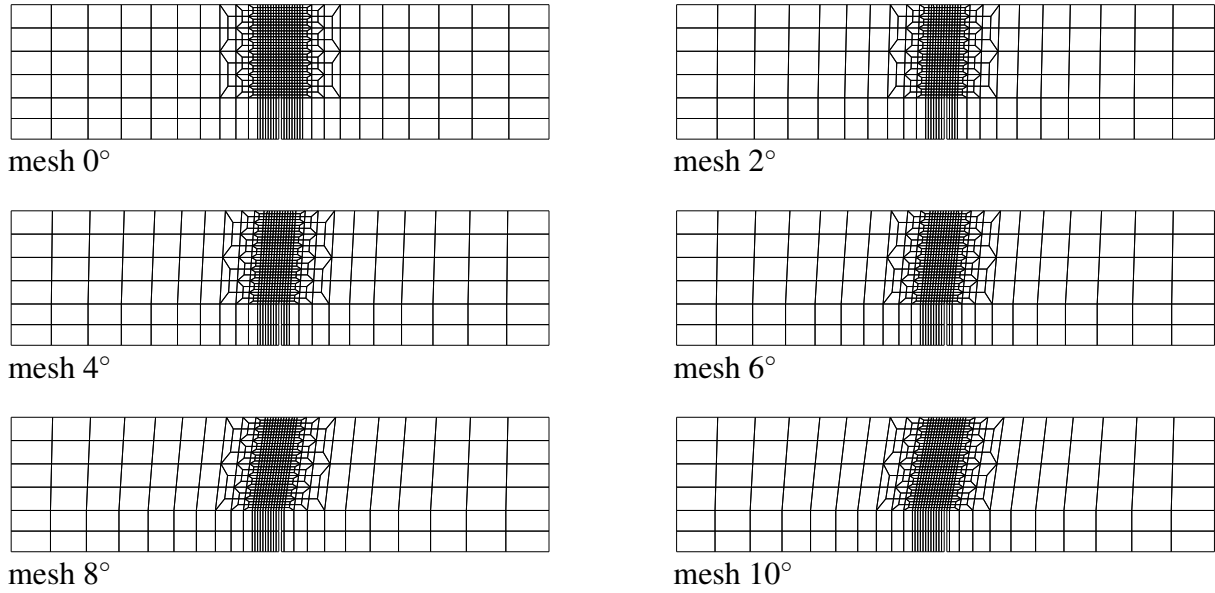


Figure 9: Finite element analysis of a notched concrete beam: Finite element discretizations

For the discretizations with a  $2^\circ$  and  $4^\circ$  bias, a straight crack path following one row of (skew) elements is observed. If the mesh bias is increased (meshes  $6^\circ$  to  $10^\circ$ ), the computed crack path follows more than one row of elements. In all cases, a slight mesh dependence of the computed crack path is observed.

In Figure 11 the distribution of the internal variable  $\alpha$  representing the state of cracking obtained from the classical fracture energy based smeared crack model using a consistent characteristic length according to OLIVER is illustrated. From comparing Figures 11 and 10 it is concluded, that both finite element formulations lead to almost identical results. To demonstrate the influence of the mesh bias on the numerical results, the load-displacement diagrams are shown in Fig. 12. Although the results obtained from the SDA-based crack model (Fig. 12a) show a slightly smaller scatter for different meshes compared to the standard smeared crack approach, the results from both finite element formulations are influenced by the mesh bias. Consequently, the influence of the mesh bias is not eliminated completely by means of embedded discontinuity models without enforcing crack path continuity..

Next, a re-analysis of the notched beam using 4 node quadrilateral elements is performed. Fig. 13 shows the distribution of the crack width  $|\zeta|$  obtained from the embedded displacement discontinuity model. The results are similar to those computed by means of triangular elements (Fig. 10).

In Fig. 14 the distribution of the internal variable  $\alpha$  representing the cracking state obtained from the smeared crack model is illustrated. Similar to the results computed by means of triangular elements, both cracking models predict an almost identical crack path. To estimate the influence of the mesh bias quantitatively, the load-displacement diagrams are shown in Fig. 15. The results obtained from the quadrilateral elements are in good agreement compared to those of the triangular discretizations. The results from both models are not independent with respect to the mesh bias.

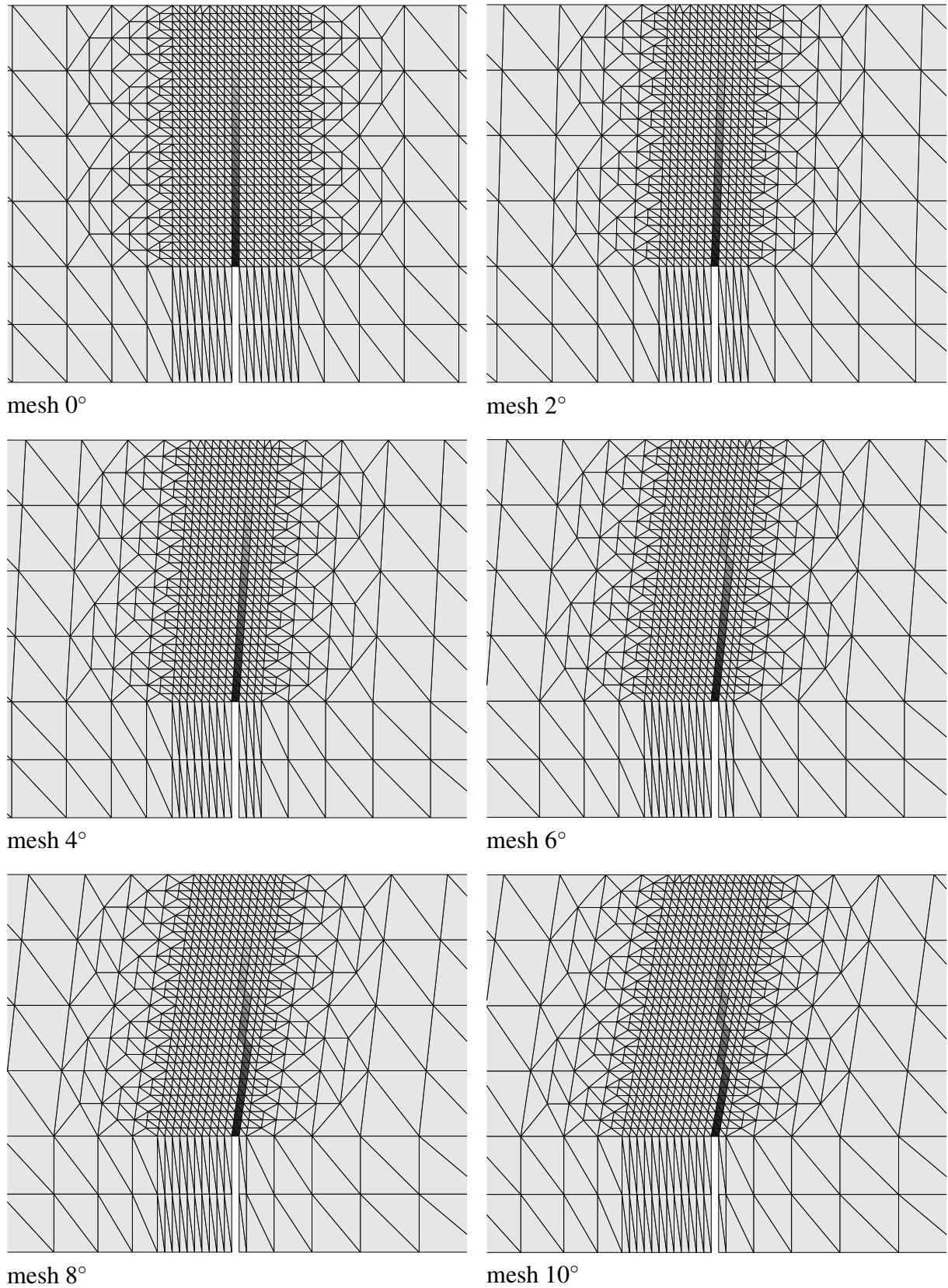


Figure 10: Finite element analysis of a notched concrete beam: Distribution of the internal variable  $|\zeta|$  representing the crack width obtained from the SDA-based crack model

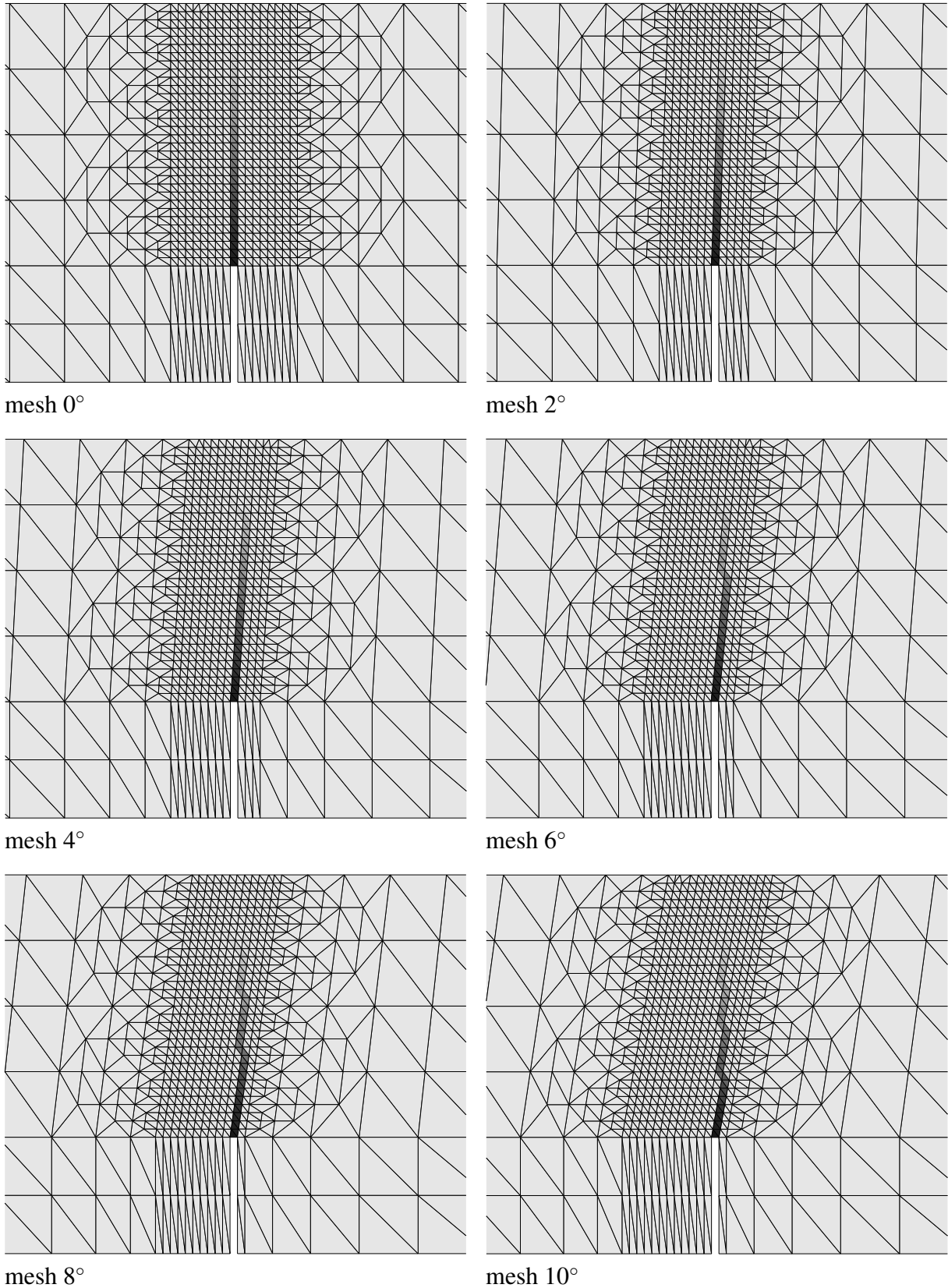


Figure 11: Finite element analysis of a notched concrete beam: Distribution of the internal variable  $\alpha$  obtained from the fracture energy based smeared crack model using a consistent characteristic length according to OLIVER

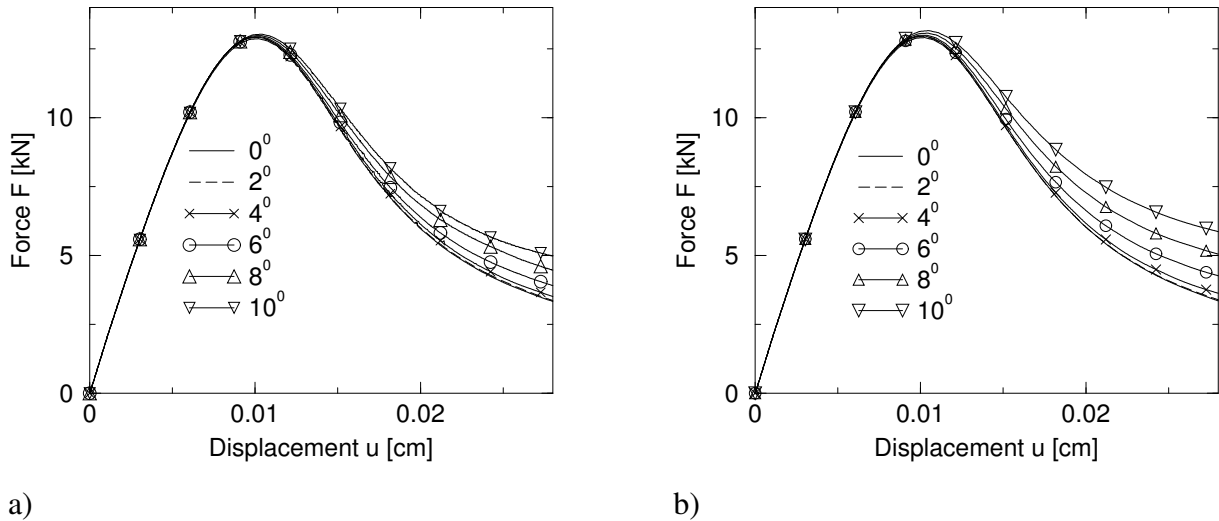


Figure 12: Finite element analysis of a notched concrete beam (CST elements): a) Load-displacement diagram obtained from the SDA-based model; b) Load-displacement diagram obtained from the fracture energy based smeared crack model using a consistent characteristic length according to OLIVER

## 6.2 L-shaped slab

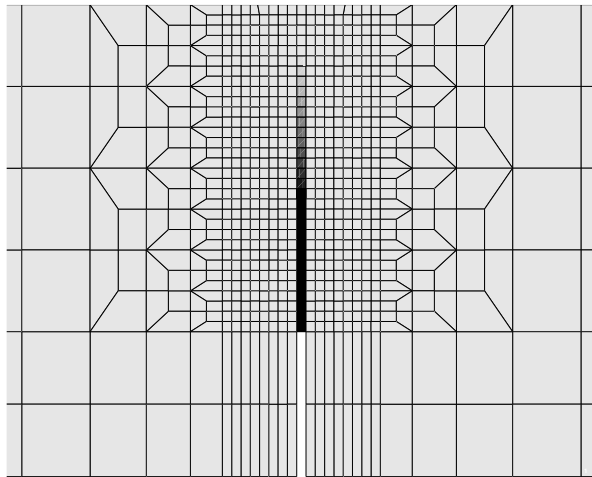
This subsection is concerned with comparative numerical analyses of an L-shaped slab by means of the embedded crack and the fracture energy based smeared crack model. The geometry of the slab and material parameters used in the analyses are contained in Figure 16. The RANKINE model is used for the modeling of crack opening. The post-peak response is controlled by an exponential softening law  $q(\alpha) = f_{tu} \exp[-\alpha/\alpha_u]$  with a fracture energy assumed as  $G_f = 0.1 \text{ kN/m}^2$ . In contrast to the numerical analyses of the notched concrete beam, only quadrilateral elements are used.

For the assessment of mesh dependence, 4 different discretizations are used. Four displacement controlled analyses are performed by means of 48, 114, 261 and 642 4 node plane stress elements (Fig. 17). Each of the finite element meshes is analyzed by employing both the SDA based and the smeared crack formulation. Loading was applied by prescribing vertical displacements at all nodes along the right edge of the slab. Convergence is checked according to the criterion (52) setting  $tol = 1.0 \cdot 10^{-8}$ .

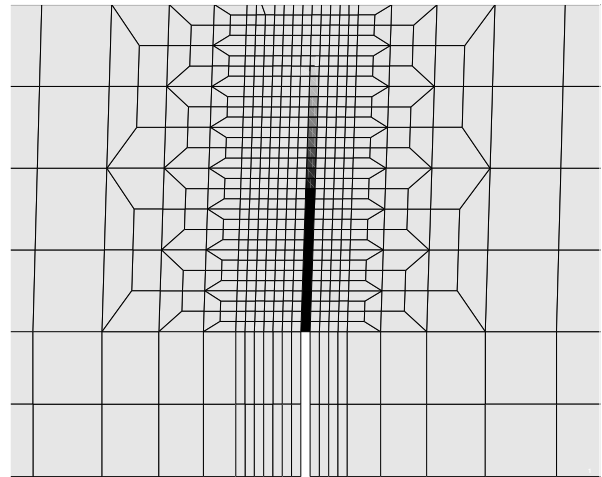
Figure 18 shows the distribution of the crack width  $|\zeta|$  and the internal variable  $\alpha$  obtained from the SDA formulation and the classical smeared crack model, respectively. Both models result in a straight crack path for the discretizations I, II and III. For a more refined discretization (mesh IV), a slightly curved crack, which starts at the corner of the slab, is predicted. While the results for meshes I, II and III are identical for both models, a slightly more curved crack path is obtained from the SDA based crack model in the vicinity of the corner for mesh IV.

In Figure 19 the structural response obtained from the SDA based and the smeared crack approach is illustrated for mesh 4. In both analyses the ultimate load is approximately predicted as 7.1 kN. In the post-peak regime the differences between the load-displacement diagrams from both investigated crack models are minimal.

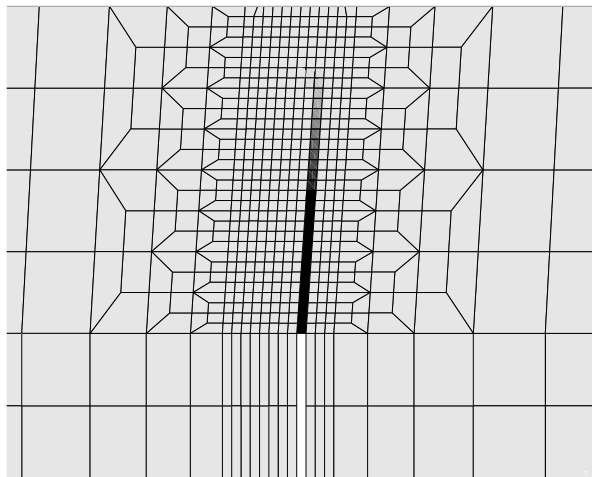
In conclusion, both formulations show more or less the same dependence of the crack path from the mesh bias, as was anticipated in Subsection 6.1.



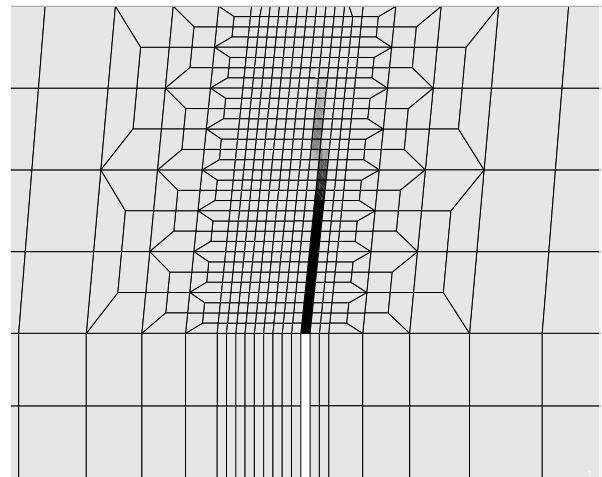
mesh 0°



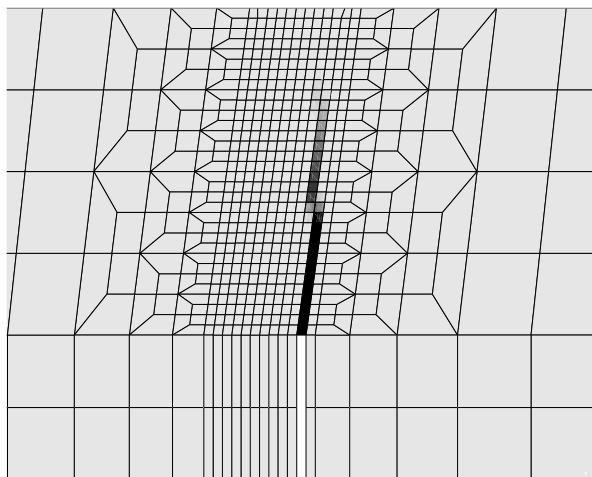
mesh 2°



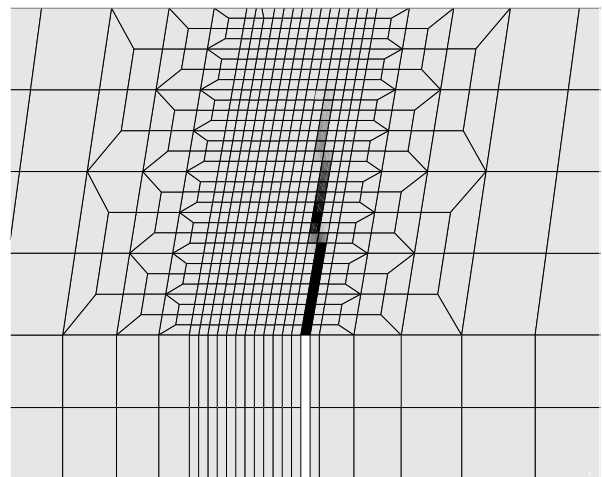
mesh 4°



mesh 6°



mesh 8°



mesh 10°

Figure 13: Finite element analysis of a notched concrete beam: Distribution of the internal variable  $|\zeta|$  representing the crack width obtained from the SDA-based crack model

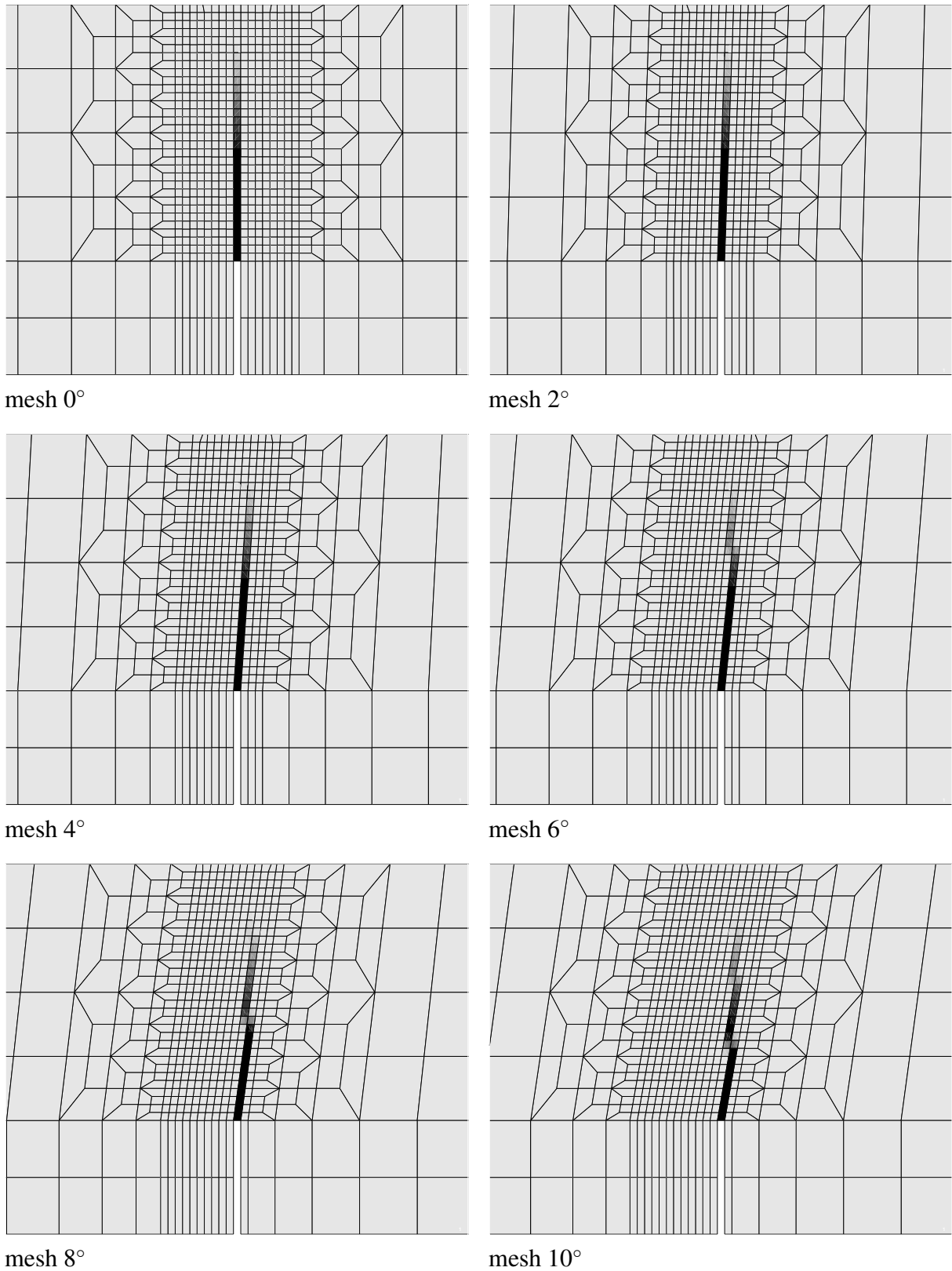


Figure 14: Finite element analysis of a notched concrete beam: Distribution of the internal variable  $\alpha$  obtained from the fracture energy based smeared crack model using a consistent characteristic length according to OLIVER

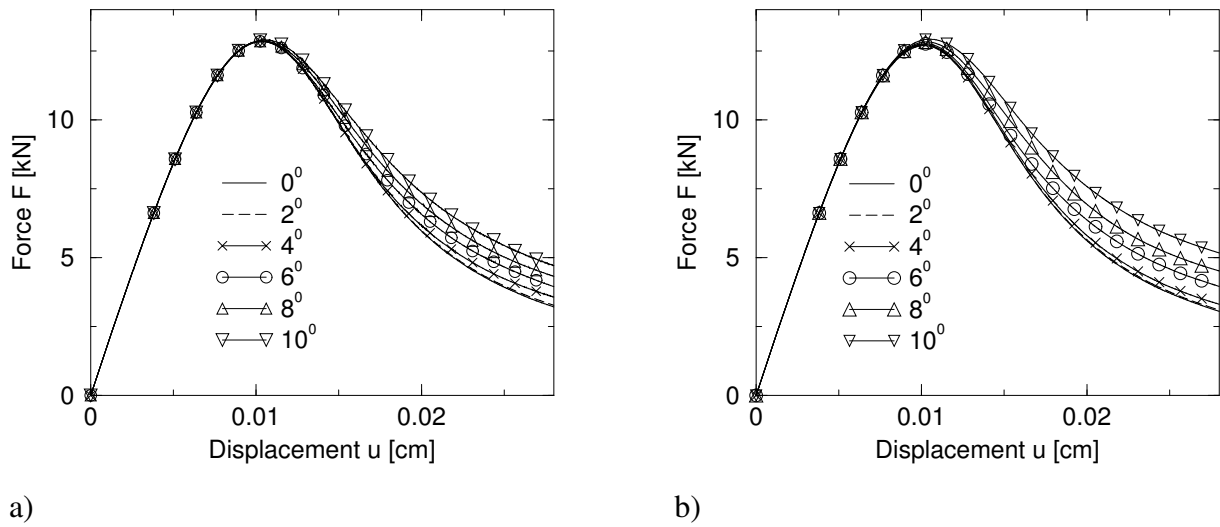


Figure 15: Finite element analysis of a notched concrete beam (4 node elements): a) Load-displacement diagram obtained from the SDA-based crack model; b) Load-displacement diagram obtained from the fracture energy based smeared crack model using a consistent characteristic length according to OLIVER

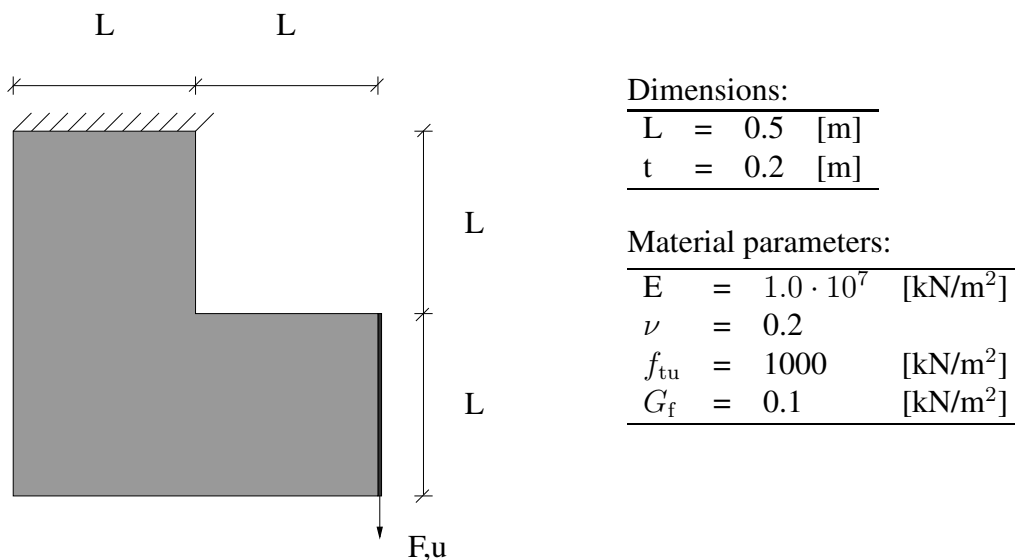
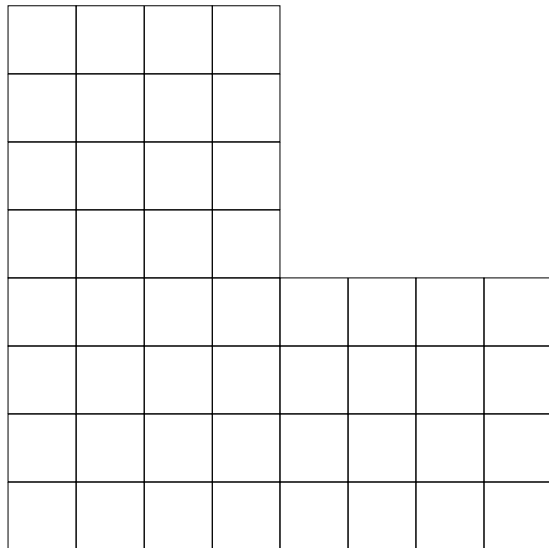
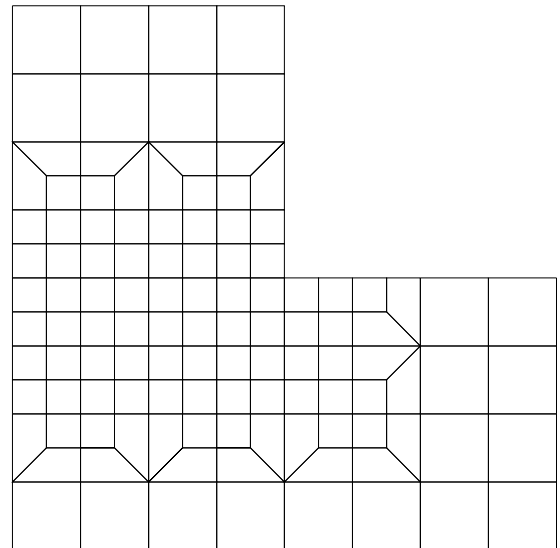


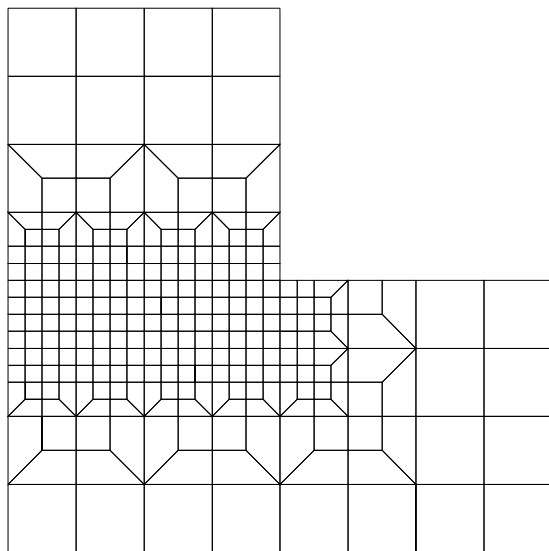
Figure 16: Finite element analyses of an L-shaped slab: Dimensions and material parameters



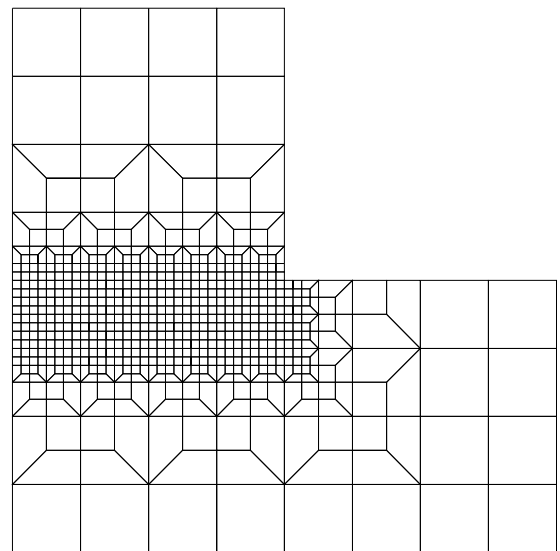
mesh I



mesh II

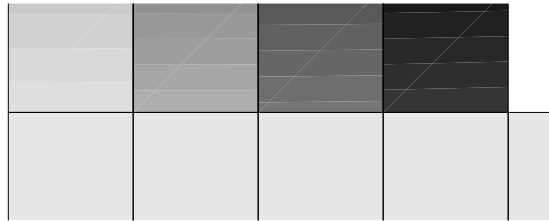


mesh III

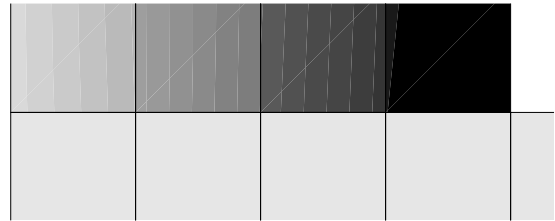


mesh IV

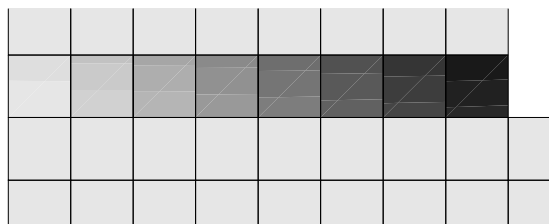
Figure 17: Finite element analyses of an L-shaped slab: Finite element discretizations using 48, 114, 261 and 642 bi-linear 4 node plane stress elements



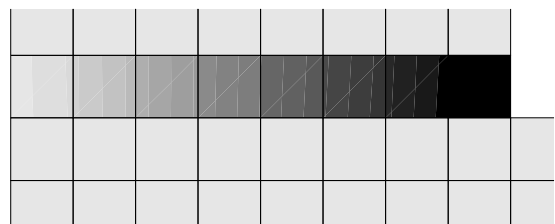
mesh I: Smeared crack model



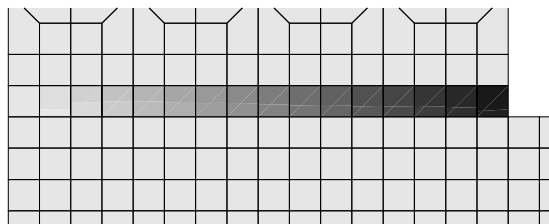
Embedded crack model



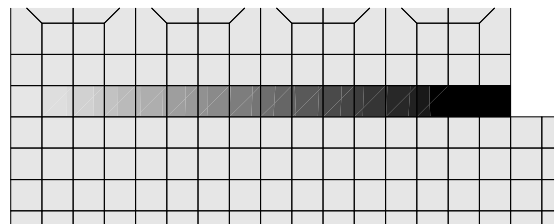
mesh II: Smeared crack model



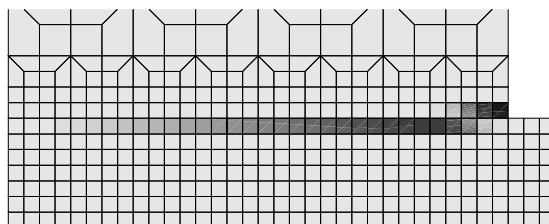
Embedded crack model



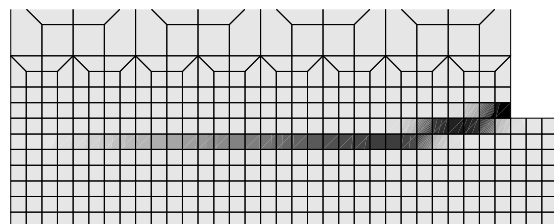
mesh III: Smeared crack model



Embedded crack model



mesh IV: Smeared crack model



Embedded crack model

Figure 18: Finite element analyses of an L-shaped slab. Left hand side: Distribution of the displacement jump  $|\zeta|$  obtained from the embedded crack model, right hand side: Distribution of the internal variable  $\alpha$  obtained from the standard smeared crack model based on the characteristic length according to OLIVER

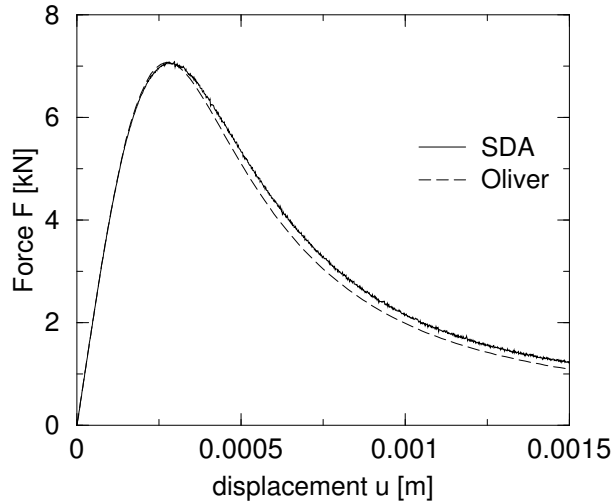


Figure 19: Finite element analyses of an L-shaped slab: Load-displacement diagram obtained from mesh 4

## 7 Conclusions

An analytical and numerical comparison of embedded strong discontinuity approaches (SDA) without enforcing crack path continuity with fracture energy based smeared crack models (SCM) has been performed in the paper. Particularly, the influence of the mesh bias of the finite element discretization on the numerically computed results obtained from both models has been investigated.

A comparison of the SDA employing a rotating crack formulation according to [22] with fracture energy smeared crack models based on the characteristic length suggested by OLIVER [25] has shown, that for constant strain finite elements, the softening response is identical for both models at the onset of localization independent of the crack direction and crack path continuity. For fixed crack formulations, it was shown analytically, that the softening response from both models are closely related. This result also holds for other existing (EAS-) formulations of the SDA [2, 7, 15, 28, 34, 40], since for constant strain elements, assuming fixed orientations of the cracks, the formulation according to [22] and the existing EAS formulations of the SDA are completely equivalent on the element level. Although the resulting stresses obtained from single finite element analyses are not necessarily identical, the equivalent softening response for both models at the onset of localization is an analytical indicator for a similar performance in structural failure analyses.

To demonstrate this equivalence in structural computations, two ultimate load analyses using different finite element discretizations by means of plane stress 3 node CST elements as well as 4 node quadrilateral elements have been performed. From these analyses, it is concluded that the concept of embedded displacement discontinuities without enforcing crack path continuity is not completely independent with respect to the mesh orientation. The mesh bias of the SDA (without crack path continuity) and the mesh bias of the fracture energy based smeared crack model using the characteristic length according to OLIVER [25] is almost identical.

The similar evolution of softening response is restricted to isotropic materials. The characteristic length concept according to OLIVER is based on a modification of the softening modulus via the scalar valued variable  $l_c$  and consequently, this approach is restricted to isotropy. In contrast, the embedded displacement discontinuity approach is based on a tensor of enhanced strains, which allows its application also for analyses of anisotropic materials.

## 8 Appendix

This Appendix contains an analytical comparison between the SDA and a fracture energy based smeared crack model using the consistent characteristic length according to OLIVER. In contrast to Section 5, attention is restricted to fixed crack approaches. Consequently, the normal vector of the crack surface is assumed as constant ( $\dot{\mathbf{n}} = \mathbf{0}$ ). For the sake of simplicity, a plane stress state is considered. However, the extension to the three-dimensional case follows identical lines.

For both models, the space of admissible stresses after the onset of cracking is postulated by means of

$$\mathbb{E}\boldsymbol{\sigma} = \{(\boldsymbol{\sigma}, q) \mid \phi = (\mathbf{n} \otimes \mathbf{n}) : \boldsymbol{\sigma} - q \leq 0 \wedge (\mathbf{n} \otimes \mathbf{m}) : \boldsymbol{\sigma} = 0\}, \quad (53)$$

with the unit normal vector  $\mathbf{n}$  of the crack surface and a unit tangential vector  $\mathbf{m}$  ( $\mathbf{m} \cdot \mathbf{n} = 0$ ). In addition to the failure surface  $\phi$  governing the normal component of the crack opening, the restriction  $(\mathbf{n} \otimes \mathbf{m}) : \boldsymbol{\sigma} = 0$  equivalent to a shear retention factor set to zero is enforced [22]. Hence, shear components of the traction vector vanish.

In the following, the first inelastic load step of a finite element analysis is considered. According to the spectral decomposition theorem, the stress tensor is written in the format

$$\boldsymbol{\sigma}^{\text{tr}} = \sigma_{(n)}^{\text{tr}} (\mathbf{n} \otimes \mathbf{n}) + \sigma_{(m)}^{\text{tr}} (\mathbf{m} \otimes \mathbf{m}). \quad (54)$$

Assuming associative evolution equations, the increment of the plastic strains for the smeared crack model is obtained as

$$\Delta \boldsymbol{\varepsilon}^{\text{P}} = (\mathbf{n} \otimes \mathbf{n}) \Delta \lambda^{(n)} + (\mathbf{m} \otimes \mathbf{n})^{\text{sym}} \Delta \lambda^{(m)}. \quad (55)$$

In Eq. (55)  $\lambda^{(n)}$  represents a plastic multiplier associated with the crack opening and  $\lambda^{(m)}$  denotes a plastic multiplier corresponding to shear sliding, respectively. Inserting the evolution (55), together with Eq. (54) into the discrete yield condition  $\phi = 0$  yields

$$\begin{aligned} \phi &= (\mathbf{n} \otimes \mathbf{n}) : \boldsymbol{\sigma}^{\text{tr}} - \underbrace{(\mathbf{n} \otimes \mathbf{n}) : \mathbb{C} : (\mathbf{n} \otimes \mathbf{n})}_{g_{11}} \Delta \lambda^{(n)} \\ &\quad - \underbrace{(\mathbf{n} \otimes \mathbf{n}) : \mathbb{C} : (\mathbf{m} \otimes \mathbf{n})}_{g_{12}} \Delta \lambda^{(m)} - q(\Delta \lambda^{(n)}) = 0 \end{aligned} \quad (56)$$

Analogously, the condition of the shear traction component  $(\mathbf{m} \otimes \mathbf{n}) : \boldsymbol{\sigma} = 0$  results in

$$\underbrace{(\mathbf{m} \otimes \mathbf{n}) : \mathbb{C} : (\mathbf{n} \otimes \mathbf{n})}_{g_{21}} \Delta \lambda^{(n)} + \underbrace{(\mathbf{m} \otimes \mathbf{n}) : \mathbb{C} : (\mathbf{m} \otimes \mathbf{n})}_{g_{22}} \Delta \lambda^{(m)} = 0. \quad (57)$$

In Eq. (56) and (57)  $g_{ij}$  denote the components of the metric tensor of  $\partial \mathbb{E}\boldsymbol{\sigma}$  assuming perfect plasticity. For the considered material model  $\mathbf{m} \cdot \mathbf{n} = 0$  holds, resulting in  $g_{12} = g_{21} = 0$ . As a consequence, Eqs. (56) and (57) are uncoupled. Hence, the softening response depends only on Eq. (56). With  $g_{12} = 0$ , Eq. (56) is rewritten as

$$(\mathbf{n} \otimes \mathbf{n}) : \boldsymbol{\sigma}^{\text{tr}} - g_{11} \Delta \lambda^{(n)} - q(\Delta \lambda^{(n)}) = 0. \quad (58)$$

In analogy to Section 5, a linear softening response of the format  $q(\Delta \lambda^{(n)}) = f_{\text{tu}} - H_{\zeta} l_c \Delta \lambda^{(n)}$  is adopted. The closed form solution of the plastic multiplier yields

$$\Delta \lambda^{(n)} = \frac{\phi^{\text{tr}}}{g_{11} - H_{\zeta} l_c} \quad \text{with} \quad \phi^{\text{tr}} = (\mathbf{n} \otimes \mathbf{n}) : \boldsymbol{\sigma}^{\text{tr}} - f_{\text{tu}}. \quad (59)$$

Next, the SDA-based cracking model is investigated [22]. Similar to Section 5, the crack opening width  $\zeta^{(n)}$  is governed by the conjugated stress  $\boldsymbol{\sigma} : (\mathbf{n} \otimes \mathbf{n})$ . Since an additional restriction for the shear component  $\boldsymbol{\sigma} : (\mathbf{m} \otimes \mathbf{n})$  has been postulated, the energy conjugated displacement jump  $\zeta^{(m)}$  has to be introduced. Consequently, the displacement jump is obtained as

$$\llbracket \mathbf{u} \rrbracket = \zeta^{(n)} \mathbf{n} + \zeta^{(m)} \mathbf{m} \quad (60)$$

and the regularly distributed enhanced strains result in

$$\Delta \tilde{\boldsymbol{\varepsilon}} = (\mathbf{n} \otimes \nabla \varphi)^{\text{sym}} \Delta \zeta^{(n)} + (\mathbf{m} \otimes \nabla \varphi)^{\text{sym}} \Delta \zeta^{(m)}. \quad (61)$$

Inserting Eqs. (54) and (61) into the yield surfaces (53), together with a linear softening response of the format  $q(\zeta^{(n)}) = f_{\text{tu}} - H_{\zeta} \zeta^{(n)}$  yields

$$\begin{aligned} \phi^{\text{tr}} - g_{11} \Delta \zeta^{(n)} - g_{12} \Delta \zeta^{(m)} + H_{\zeta} \Delta \zeta^{(n)} &= 0 \\ g_{21} \Delta \zeta^{(n)} + g_{22} \Delta \zeta^{(m)} &= 0, \end{aligned} \quad (62)$$

with the coefficients

$$\begin{aligned} g_{11} &= (\mathbf{n} \otimes \mathbf{n}) : \mathbb{C} : (\mathbf{n} \otimes \nabla \varphi) & g_{12} &= (\mathbf{n} \otimes \mathbf{n}) : \mathbb{C} : (\mathbf{m} \otimes \nabla \varphi) \\ g_{21} &= (\mathbf{m} \otimes \mathbf{n}) : \mathbb{C} : (\mathbf{n} \otimes \nabla \varphi) & g_{22} &= (\mathbf{m} \otimes \mathbf{n}) : \mathbb{C} : (\mathbf{m} \otimes \nabla \varphi). \end{aligned} \quad (63)$$

In contrast to the smeared crack model,  $g_{12} \neq 0$  in general. Eliminating  $\zeta^{(m)}$ , Eqs. (62) results in

$$\phi^{\text{tr}} - \left[ g_{11} - \underbrace{\frac{g_{12} g_{21}}{g_{22}}}_{\tilde{g}_{11}} \right] \Delta \zeta^{(n)} + H_{\zeta} \Delta \zeta^{(n)} = 0, \quad (64)$$

and

$$\Delta \zeta^{(n)} = \frac{\phi^{\text{tr}}}{(g_{11} - \tilde{g}_{11}) - H_{\zeta}}, \quad (65)$$

respectively. From a comparison of Eq. (65) and (59), it is concluded that the difference between the softening evolution of the smeared crack model and the SDA-based approach depends on the coefficient  $\tilde{g}_{11}$ . For the case of HOOKE's law, the components  $g_{ij}$  are obtained as

$$\begin{aligned} g_{11} &= \mathbb{C}_{1111} (\mathbf{n} \cdot \nabla \varphi) & g_{12} &= \frac{E}{1 - \nu^2} (\mathbf{m} \cdot \nabla \varphi) \\ g_{21} &= \frac{1}{2} \frac{E}{1 + \nu} (\mathbf{m} \cdot \nabla \varphi) & g_{22} &= \frac{1}{2} \frac{E}{1 + \nu} (\mathbf{n} \cdot \nabla \varphi) \end{aligned} \quad (66)$$

and consequently, the ratio between  $g_{11}$  and  $\tilde{g}_{11}$  is computed as

$$\frac{\tilde{g}_{11}}{g_{11}} = \nu \left( \frac{\mathbf{m} \cdot \nabla \varphi}{\mathbf{n} \cdot \nabla \varphi} \right)^2. \quad (67)$$

According to Eq. (67), this ratio depends on the POISSON's ratio  $\nu$  as well as on a geometrical factor. For equilateral triangle elements the estimate

$$\left( \frac{\mathbf{m} \cdot \nabla \varphi}{\mathbf{n} \cdot \nabla \varphi} \right)^2 \leq \frac{1}{3} \quad (68)$$

holds. Since for concrete  $\nu$  is approximately equal to 0.2, the final estimate

$$\frac{\tilde{g}_{11}}{g_{11}} \leq \frac{1}{15} \quad (69)$$

is obtained. Consequently, the softening response of the smeared crack model is closely related to that of the SDA-based cracking model, also if a fixed crack approach is adopted.

## References

- [1] J. Alfaiate, G. N. Wells, and L. J. Sluys. On the use of embedded discontinuity elements with path continuity for mode-i and mixed-mode fracture. *Engineering Fracture Mechanics*, 69(6):661–686, 2002.
- [2] F. Armero and K. Garikipati. Recent advances in the analysis and numerical simulation of strain localization in inelastic solids. In D.R.J. Owen, E Oñate, and E. Hinton, editors, *Proc., 4th Int. Conf. Computational Plasticity*, volume 1, pages 547–561, 1995.
- [3] F. Armero and K. Garikipati. An analysis of strong discontinuities in multiplicative finite strain plasticity and their relation with the numerical simulation of strain localization in solids. *International Journal for Solids and Structures*, 33:2863–2885, 1996.
- [4] I. Babuška and J.M. Melenk. The partition of unity method. *International Journal for Numerical Methods in Engineering*, 40:727–758, 1997.
- [5] Z.P. Bažant and G. Pijaudier-Cabot. Nonlocal damage, localization, instability and convergence. *Journal of Applied Mechanics*, 55:287–293, 1988.
- [6] R.I. Borja. A finite element model for strain localization analysis of strongly discontinuous fields based on standard galerkin approximation. *Computer Methods in Applied Mechanics and Engineering*, 190:1529–1549, 2000.
- [7] R.I. Borja and A.R. Regueiro. Strain localization in frictional materials exhibiting displacement jumps. *Computer Methods in Applied Mechanics and Engineering*, 190:2555–2580, 2001.
- [8] W.F. Chen and D.J. Han. *Plasticity for structural engineers*. Springer, New-York, Berlin, Heidelberg, 1988.
- [9] M. A. Crisfield. Difficulties with current numerical models for reinforced concrete and some tentative solutions. In F. Damjanicm, E. Hinton, D. R. J. Owen, N. Bićanic, and V. Simovic, editors, *Int. Conf. on Computer-Aided Analysis and Design of Concrete Structures*, pages 331–358. Pineridge Press, Swansea, 1984.
- [10] R. De Borst. Simulation of strain localization: A reappraisal of the cosserat continuum. *Engineering Computations*, 8:317–332, 1991.
- [11] R. De Borst. Some recent issues in computational mechanics. *International Journal for Numerical Methods in Engineering*, 52:63–95, 2001.
- [12] R. De Borst and H.B. Mühlhaus. Gradient-dependent plasticity: Formulation and algorithmic aspects. *International Journal for Numerical Methods in Engineering*, 35:521–539, 1992.
- [13] K. Garikipati. *On strong discontinuities in inelastic solids and their numerical simulation*. PhD thesis, Stanford University, 1996.
- [14] M. Jirásek. Numerical modeling of deformation and failure of materials. *Lecture notes*, 1999.

- 
- [15] M. Jirásek and T. Zimmermann. Embedded crack model: Part I: Basic formulation, Part II: Combination with smeared cracks. *International Journal for Numerical Methods in Engineering*, 50:1269–1305, 2001.
- [16] C. Johnson and R. Scott. A finite element method for problems in perfect plasticity using discontinuous trial functions. In W. Wunderlich, E. Stein, and K.J. Bathe, editors, *Nonlinear finite element analysis in structural mechanics*, pages 307–324, 1981.
- [17] J. Lubliner. *Plasticity theory*. Maxwell Macmillan International Edition, 1997.
- [18] N. Moës, J. Dolbow, and T. Belytschko. A finite element method for crack growth without remeshing. *International Journal for Numerical Methods in Engineering*, 46:131–150, 1999.
- [19] J. Mosler. *Finite Elemente mit sprungstetigen Abbildungen des Verschiebungsfeldes für numerische Analysen lokalisierter Versagenszustände in Tragwerken*. PhD thesis, Ruhr University Bochum, 2002.
- [20] J. Mosler and G. Meschke. 3D FE analysis of cracks by means of the strong discontinuity approach. In E. Oñate, G. Bugada, and B. Suárez, editors, *European Congress on Computational Methods in Applied Sciences and Engineering*, 2000.
- [21] J. Mosler and G. Meschke. A comparison of embedded discontinuity approaches with fracture energy based smeared crack models. In *Fifth World Congress on Computational Mechanics*, 2002.
- [22] J. Mosler and G. Meschke. 3D modeling of strong discontinuities in elastoplastic solids: Fixed and rotating localization formulations. *International Journal for Numerical Methods in Engineering*, 2003. in press.
- [23] H.B. Mühlhaus and E.C. Aifantis. A variational principle for gradient plasticity. *International Journal for Solids and Structures*, 28:845–857, 1991.
- [24] E. Oñate, S. Oller, J. Oliver, and J. Lubliner. A constitutive model for cracking of concrete based on the incremental theory of plasticity. In D. R. J. Owen, E. Hinton, and E. Oñate, editors, *Int. Conf. on Computational Plasticity, Models, Software and Applications*, pages 1311–1330. Pineridge Press, Swansea, 1987.
- [25] J. Oliver. A consistent characteristic length for smeared cracking models. *International Journal for Numerical Methods in Engineering*, 28:461–474, 1989.
- [26] J. Oliver. Continuum modelling of strong discontinuities in solid mechanics. In D.R.J. Owen, E. Oñate, and E. Hinton, editors, *Proc., 4th Int. Conf. Computational Plasticity*, volume 1, pages 455–479, 1995.
- [27] J. Oliver. Continuum modelling of strong discontinuities in solid mechanics using damage models. *Computational Mechanics*, 17(1-2):49–61, 12 1995.
- [28] J. Oliver. Modelling strong discontinuities in solid mechanics via strain softening constitutive equations part 1: Fundamentals. part 2: Numerical simulations. *International Journal for Numerical Methods in Engineering*, 39:3575–3623, 1996.

- 
- [29] J. Oliver and J. Simo. Modelling strong discontinuities in solid mechanics by means of strain softening constitutive equations. In H. Mang, N. Bićanić, and R. de Borst, editors, *Computational Modelling of concrete structures*, pages 363–372. Pineridge press, 1994.
- [30] S. Pietruszczak and Z. Mroź. Finite element analysis of deformation of strain-softening materials. *International Journal for Numerical Methods in Engineering*, 17:327–334, 1981.
- [31] G. Pijaudier-Cabot and Z.P. Bažant. Nonlocal damage theory. *Journal of Engineering Mechanics (ASCE)*, 113:1512–1533, 1987.
- [32] A.R. Regueiro and R.I. Borja. A finite element method of localized deformation in frictional materials taking a strong discontinuity approach. *Finite Elements in Analysis and Design*, 33:283–315, 1999.
- [33] J. Simo and T.J.R. Hughes. *Computational inelasticity*. Springer, New York, 1998.
- [34] J. Simo and J. Oliver. A new approach to the analysis and simulation of strain softening in solids. In Z.P. Bažant, Z. Bittnar, M. Jirásek, and J. Mazars, editors, *Fracture and Damage in Quasibrittle Structures*, pages 25–39. E. &F.N. Spon, London, 1994.
- [35] J. Simo, J. Oliver, and F. Armero. An analysis of strong discontinuities induced by strain softening in rate-independent inelastic solids. *Computational Mechanics*, 12:277–296, 1993.
- [36] J.C. Simo and F. Armero. Geometrically non-linear enhanced strain mixed methods and the method of incompatible modes. *International Journal for Numerical Methods in Engineering*, 33:1413–1449, 1992.
- [37] J.C. Simo and S. Rifai. A class mixed assumed strain methods and the method of incompatible modes. *International Journal for Numerical Methods in Engineering*, 29:1595–1638, 1990.
- [38] P. Steinmann and K.J. Willam. Localization within the framework of micropolar elastoplasticity. In V. Mannl, J. Najar, and O. Brüller, editors, *Advances in continuum mechanics*, pages 296–313. Springer, Berlin-Heidelberg, 1991.
- [39] G.N. Wells and L.J. Sluys. Analysis of slip planes in three-dimensional solids. *Computer Methods in Applied Mechanics and Engineering*, 190:3591–3606, 2001.
- [40] G.N. Wells and L.J. Sluys. Three-dimensional embedded discontinuity model for brittle fracture. *International Journal for Solids and Structures*, 38:897–913, 2001.